Hyporheic exchange and residence time distribution

in the Petit Buëch river in France

Uranine dye experiment in the Petit Buëch river.

Master Thesis

Emmy Zwier
Supervisor: M. van der Perk
Co-supervisor: M.R. Hendriks

Department of Physical Geography
Faculty of Geosciences
Utrecht University, The Netherlands

March 2014

Abstract

Hyporheic exchange and residence times are important for the response and prediction of hydrologic systems for both natural and human-induced changes. Understanding residence times of particles in the hyporheic zone is important for understanding the consequences of e.g. climate change, industrial pollution, and fertilizers for agriculture, aquatic life, and human water supply. The main challenge in understanding contaminant migration is characterisation of hyporheic zone water flow paths that differ in length and duration. Data that were collected for modeling of hyporheic exchange were: hydraulic heads, digital elevations, Darcy velocities, porosities, travel times, and the thickness of the water-bearing layer. Modeling of hyporheic flow and particle tracking was done with Modflow and PmPath. The program ArcGIS was used for the visualisation of data.

The fluctuation of the river discharge and water level resulted in variable locations of river water infiltration locations and rates. A small river discharge resulted in large quantities of river water infiltration which could be more than 50% of the total river discharge. Furthermore, the variation in residence times and hyporheic exchange rates were due to the varying morphology of the point bar. As a result of long residence times, the hyporheic zone was able to retain large quantities of solutes from stream water. Therefore, chemical signals due to e.g. precipitation, industrial pollution, or agriculture may be delayed or even attenuated by hyporheic zone exchange.

Preface & acknowledgements

This master thesis is part of the MSc track Hydrology from the master specialisation programme Earth Surface and Water at Utrecht University in the Netherlands.

First of all, I would like to thank my supervisor dr. M. van der Perk for his support and advice during this research. Furthermore, I am thankful to H. Markies for helping installing monitoring wells, instructing the dGPS device, and for making aerial photographs. I would also like to thank H. van der Meer for providing the Abem SAS 300C for resistivity measurements, B. van Dam for giving fluorimeter instructions, M. van Maarseveen for instructing the dGPS device, and W. Marra for generating the high resolution georeferenced orthophoto and digital elevation model. Finally, I wish to thank my family and friends for support and help and for their great company during the field work.

Table of contents

List of figures

List of tables

List of appendices

Chapter 1 Introduction

1.1 Hyporheic zone & residence times

An understanding of hydrologic processes for human-induced changes and associated responses is important to understand the ecological effects of polluted surface water, as well for decision planning in water management. Surface water and groundwater are important resources for, for instance drinking water, industry, irrigation, and crop cultivation. Surface water and groundwater ecosystems show the response of human-induced changes and the related sustainability issues. Human activities often threaten the hydrological and biological conditions of a river basin by polluting surface water. Furthermore discharge of saline or low-quality groundwater into surface water may result in a quality decline of the latter (Sophocleous, 2002). The exchange between surface water and groundwater affects the transport and fate of contaminants and other substances in streams (Salehin et al., 2004). The region where surface water and groundwater are mixed is also called the hyporheic zone (Boulton, 2007).

Most hydrological and ecological research has treated groundwater and rivers separately. Groundwater is mostly defined by long residence times, unchanging morphology and laminar flow. In contrast, rivers are marked by turbulence, short residence times, variable discharge, unidirectional transport of nutrients and sediments, and a dynamic morphology (Brunke and Gonser, 1997). Just recently more attention is paid to the processes at the interface between groundwater and river environments because researchers now recognize that there is exchange of water, nutrients and sediments between surface streams and groundwater.

Water and solutes which travel through the hyporheic zone may undergo processes such as transformation, degradation, or adsorption to fine sediments (Boulton et al., 1998). The type and degree of processes which have an effect on solutes depend on their residence time in the hyporheic zone. Industrial sewage discharge to rivers can significantly increase nutrient concentrations which may result in a change of hyporheic conditions through, for example, the depletion of oxygen. In addition, anthropogenic nutrients, pesticides, and heavy metals can move from groundwater into surface water (Boulton et al., 1998).

To increase the understanding of hydrologic processes researchers and managers need information on the mechanisms by which energy and materials are transferred in the

hyporheic zone. The quantification of the residence time distribution provides a good insight in the hydro-biogeochemical system (Wolock et al., 1997).

The hyporheic zone is defined by hyporheic exchange and circulation cells that move surface water into the sediment and back to the river. A hyporheic zone includes riverbeds, riverbanks, saturated sediments under exposed bars, and floodplains. The hyporheic zone may be as thick as tens of meters and as wide as hundreds of meters (Tonina and Buffington, 2009).

The definition of the hyporheic exchange may be quite extensive. Most hydrologists define it as the exchange of water and solutes through sediment. Stream and groundwater exchange may be composed of three components: 1) underflow, the groundwater flux moves in the same direction as the streamflow and thus parallel to the river, 2) baseflow, the groundwater flux moves perpendicular to or from the river depending on whether the river is effluent or influent, respectively, 3) both baseflow and underflow (Larkin and Sharp, 1992).
Surface water and groundwater exchange through sediment occurs due to a combination of streambed pressure gradients and hydraulic conductivity. Streambed pressure gradients can be caused by variations in bed elevation, flow depth, flow velocity and flow momentum. Pressure head variations may also be caused by the channel sinuosity, type of channel (divided or braided), changes in channel width or slope, steady or unsteady flow, changes in reach morphology, and turbulent mixing.

Basically, hyporheic exchange is caused by downwelling of surface water and upwelling of groundwater. With downwelling, surface water and solutes are transferred into the sediment due to the presence of a high pressure zone (Tonina and Buffington, 2009). Downwelling fluxes transport high concentrations of dissolved oxygen and nutrients into the sediment. Organisms living in the sediment filter the water and reduce the biological and chemical loads (Tonina, 2005).

Surface water which infiltrates into the sediment can travel some distance before upwelling into the stream (Boulton, 2007). Upwelling occurs when there is a low pressure zone between the sediment and river water. Due to upwelling reduced elements and solutes from the hyporheic zone are transported back into the river. After flood events upwelling may be a source of nutrients and solutes to streams. As a result of down- and upwelling subsurface and surface solute concentrations will be altered which has an effect on the habitat for organisms living in the environment (Tonina, 2005).

Hyporheic exchange due to down- and upwelling is also influenced by the hydraulic conductivity. Upwelling occurs when the velocity of subsurface flow is reduced due to the reduction of the hydraulic conductivity. Opposite, an increase in the hydraulic conductivity causes larger subsurface velocities and downwelling (Tonina and Buffington, 2009). The hydraulic conductivity is influenced by characteristics of both water and sediment and is therefore dependent on the porosity and connectivity of the pores in the sediment (Hendriks, 2010).

The porosity is an important morphological, hydrological, ecological, and geological parameter. Furthermore, it is a key property of fluvial sand-gravel mixtures (Frings et al., 2008). Porosity determines for a large part the formation and shape of morphological features due to the influence on the angle of internal friction and the initiation of sediment motion. The voids between sediment particles provide space to live for organisms in the hyporheic zone (Boulton et al., 1998).

Hyporheic flow occurs in the voids between sediments and the porosity is an indicator for the residence time of water that remains in the subsurface before upwelling into the stream. The residence time is the amount of time that a particle spends in a particular system. An increase in storage capacity of the sediment will result in more water exchange between a river and the sediment (Morrice et al., 1997). The processes of how a catchment retains and releases water and solutes can be indicated by the distribution of residence times. Moreover storage, flow pathways and the source of water and solutes are determined by the catchment residence time. The residence time may be influenced by, for example, evaporation, precipitation, groundwater flow, or runoff through a stream (Fitts, 2002). Therefore catchment processes can be described by the distribution of residence times which may be an indicator of hydro-geochemical and anthropogenic events (McGuire and McDonnell, 2006).

1.2 Research objectives

The aim of this study is to obtain better knowledge of hydrologic processes occurring in the hyporheic zone and to get a better understanding of groundwater and surface water interactions in gravel-bed rivers. In order to get a better understanding, a point bar of the Petit Buëch river in France is studied. The specific objectives of this study are:

- To quantify the hyporheic exchange and rates.
- To determine the residence time distribution of water in a reach of the Petit Buëch river.

1.3 Research approach

Dye tracer experiments were carried out to determine the fluxes and residence times in the Petit Buëch river. Steady state and transient groundwater modelling were performed for determination of the fluxes and residence times in groundwater. In order to be able to parameterise the model, field observations for the porosity and the thickness of the water-bearing layer were executed. Furthermore, water level and hydraulic head measurements were performed for determination of the threshold values and initial conditions. The hydraulic conductivity was determined on several locations with salt tracer experiments. With model calibration the hydraulic conductivity was optimized.

1.4 Site description

The field work was conducted near La Bâtie Montsaléon in the region Provence-Alpes-Côte d'Azur in south-eastern France. The area is part of the department Hautes-Alpes which has Gap as its capital (figure 1.1). The exchange between surface water and groundwater was studied at a section of the hyporheic zone of the Petit Buëch River near La Bâtie Montsaléon (figures 1.2 and 1.3). The Petit Buëch originates in the cirque of Chaudun at Pic de l'Aiguille (2140 m) at the southern end of the Dévoluy massif. Several small sources converge at the valley bottom and form the Petit Buëch river. Subsequently the Petit Buëch flows in southern direction through the villages of Rabou and la Roche-des-Arnauds. Then the river turns to the southwest where it receives water from the Béoux river before flowing into the Buëch river upstream of Serres (680 m) after a course of 44.5 km. The Buëch river flows further south until it mouths into the Durance river at Sisteron (Sandre, 2011) .

Figure 1.1: Flow path of the Petit Buëch river from the cirque of Chaudun at Pic de l'Aiguille where it originates to Serres where it flows into the Buëch river.

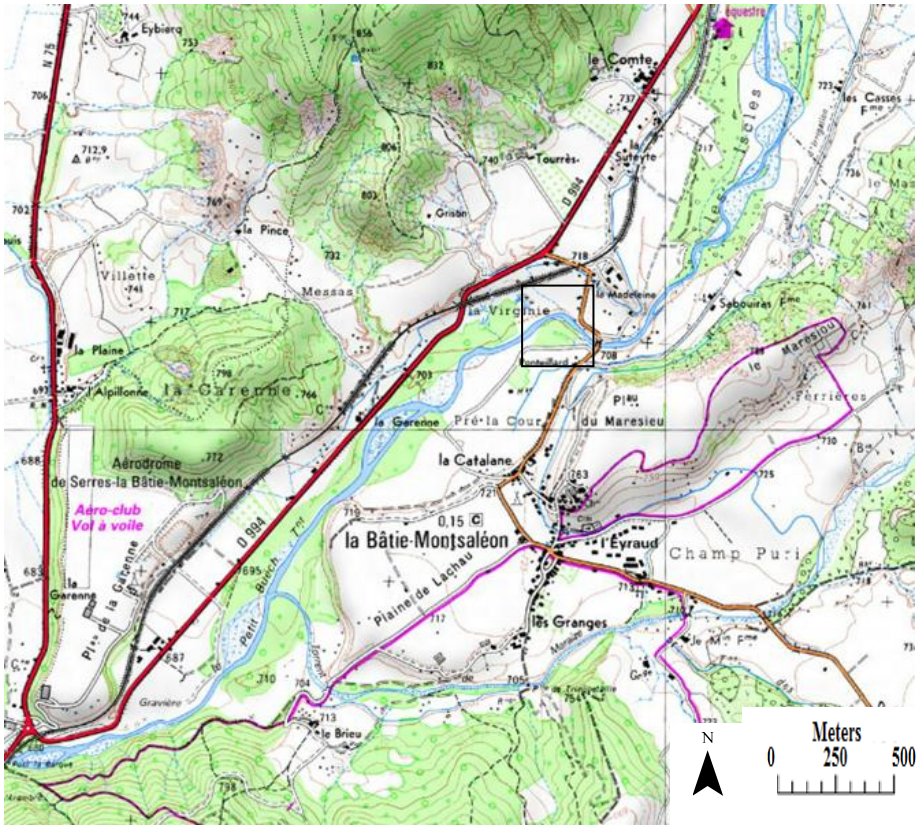

Figure 1.2: Location of the research location

near La Bâtie Montsaléon.

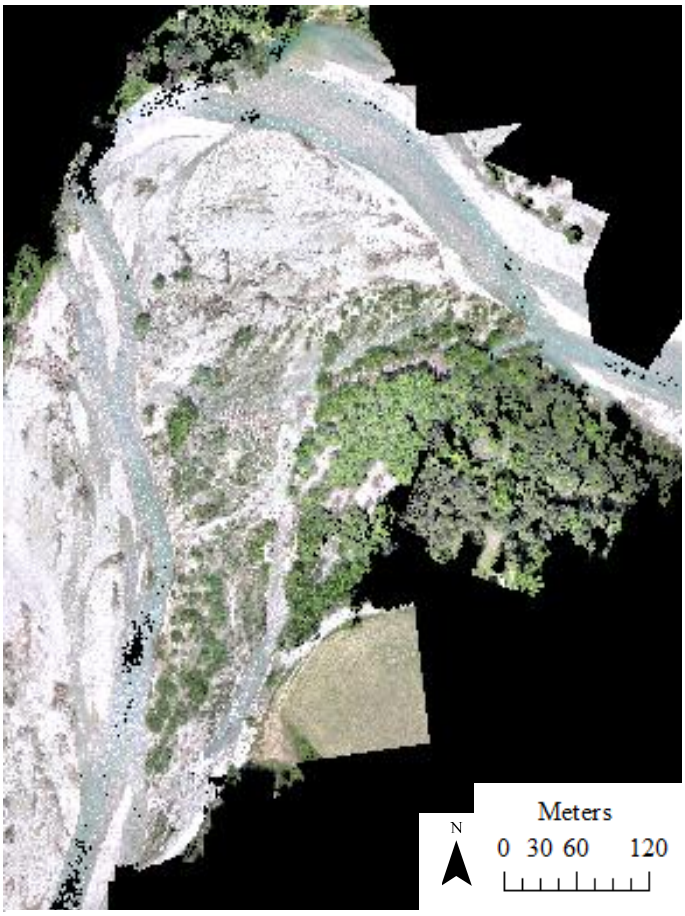

Figure 1.3: Orthophoto of the research area.

The Petit Buëch is a meandering river with depositional bars on the insides of bends (figure 1.3). Meanders develop by the erosion of banks and sedimentation on the opposite side of the channel (point bar). Meandering rivers transport a mixture of suspended load and bedload. Coarse bedload is carried in the deepest parts of the channel while fine bedload is carried at lesser channel depths. When there is enough friction by the river bottom to reduce the flow velocity bedload will be deposited (Harvey and Bencala, 1993). When bedload is repeatedly deposited close to the channel edge, it may lead to the formation of a levée which has a higher level than the floodplain. During periods of high discharge and accompanying high-stage flow, water may take short-cuts over the point bar whereby flow may become concentrated into a chute channel. Chute channels can be recognized by a scour with lateral accretion surfaces. Chute channels are mainly semi-permanent features because they are only active during periods of high discharge (Harvey and Bencala, 1993).

Geologically, the area consists mainly of hard and resistant limestone rocks and several types of softer marls. The limestone rocks were formed during the upper Malm (Calcaire Tithonique) and the lower Cretaceous (Barrémien). The softer marls were formed during the Dogger and Malm (Terres Noires) or Albian (Marnes Blues). The Terres Noires, dark marls from the early Malm with a clay content of 35 % to 65%, can be more than a kilometre thick and are highly erodible. The Calcaire Tithonique from the upper Malm is a massive limestone with almost no clay content (Debelmans, 1974). The variation of those geological units is reflected in the sediment that can be found near the Petit Buëch river. The point bar of the study area consists of a variation of limestones (75%), sands (15%), and clays (10%). Solid and larger parts of Terres Noires are hardly found due to the high erodibility which results in the disintegration into clay particles.

The research area is located in a valley and has a sub-Mediterranean climate where the locations of the mountains have a great influence on the climate. The area receives an average amount of 2700 hours of sun per year and the average yearly temperature is 12 degrees Celsius. The yearly precipitation is between 800 to 900 mm distributed over 70 to 80 rain days. The precipitation amount and wind strength largely depend on the wind direction and the location of the mountains in the surrounding area. The main wind direction is south-south-east. During December till March snow builds up at the southern end of the Dévoluy massif until it starts to melt in spring. In May and June the snowmelt results in a higher discharge of the Petit Buëch. Most of the precipitation is generated during September to November when rainstorms are common (Gaussen, 1970). During summer, there is almost no precipitation and the area is dominated by drought. The temperature is also linked to evaporation whereby evaporation has a great impact on the water balance of the soil which influences the vegetation development (Meyzeng, 1984).

The vegetation in the region is a pine, larch and spruce forest for higher altitudes. A mixed oak and beech forest alternated with grassland and agriculture covers lower altitudes. Some parts of the studied river bend are covered by shrubs, single trees, or forest.

Chapter 2 Methods

This section describes the methods used to collect and process the field measurements: hydraulic heads, porosities, hydraulic conductivity, discharges, resistivities, and surface elevations. Furthermore, the groundwater modeling methods are described: Modflow and PmPath modeling, discharges, and the residence time distribution.

2.1 Field measurements

Data was collected at the research area in order to be able to parameterise a detailed model of hyporheic zone interactions. The field measurements were done over a period of one month, in May and June 2013.

2.1.1 Hydraulic Head

The hydraulic heads were determined along transects which were placed perpendicular to the main course of the river. The hydraulic head was determined by two methods: a pit or a monitoring well. The dimensions of the monitoring wells are given in appendix A. Six transects were made with a total of 14 pits and 7 monitoring wells. For the pit method there was dug until the groundwater was reached. Hereafter a metal pin was hammered into the pit until the top of the pin was equal with the surface. The exact locations of the top of the metal pins were determined with dGPS. Therefore the pin acted as a reference point for measuring the groundwater depth. The groundwater depth was measured from the top of the pin to the water table. Monitoring wells were mostly placed at locations where the water was deep (>1.5 m) below the surface. Groundwater depths for monitoring wells were determined with a 'plopper' attached to a tape measure.

The surface water gradient was observed using three metal pins which were placed in the main course of the river upstream of the research area, downstream in the main course, and in a side stream. As for the hydraulic head measurements in pits, the top of the metal pins acted as reference points.

Most dGPS measurements along water edges were done on 6 June 2013 while head measurements were done in the period from 3 June 2013 to 19 June 2013. Therefore the head data of pits, monitoring wells and for the surface water gradients were converted to 6 June

2013 by linear interpolation. This was possible since the hydraulic head for both groundwater and surface water decreased linearly (figures 3.1 and 3.2).

2.1.2 Porosity

During the fieldwork a division was made between the sorting of the surface materials. The porosity values were based on porosity calculations performed by Grimberg (2013). Grimberg (2013) conducted field research at the same location in 2011 and determined grain size distributions of surface material throughout the area.

Grain size distributions are an indicator for the porosity and sorting of the material. The porosity [n; -] depends on the grain size distribution where the following formula is applied (Frings et al., 2008; Beard and Weyl, 1973):

$$n = 0.435 - 0.222\sigma \qquad \text{for } \sigma \leq 1.0 \qquad (1)$$

$$n = 0.341 - 0.028\sigma \qquad \text{for } \sigma > 1.0 \qquad (2)$$

Where σ is the standard deviation of the grain size distribution which was estimated by:

$$\sigma = \left(\frac{\ln(D_{16})}{\ln(2)} - \frac{\ln(D_{84})}{\ln(2)} \right) / 4 \qquad (3)$$

D_{16} and D_{84} are the 16 and 84 percentiles of the cumulative weight percent which were smaller than grain size of 16 mm and 84 mm, respectively.

Grimberg (2013) measured the grain size distribution by passing the material through sieves with different mesh sizes. For this research, the porosity division for the study area was made by combing field observations of the grain size distribution at the surface and the porosity values (ranging from 0.18 to 0.35) found by Grimberg (2013).

About 50 field observations for porosity determination were performed. For this study, the porosity values were divided into four classes: surfaces with almost only sand had a porosity of 0.18; surfaces with very bad sorting had a porosity of 0.21, surfaces with medium sorting had a porosity of 0.25; surfaces with good sorting had a porosity of 0.33. The field observations were noted as points which were subsequently interpolated with kriging to obtain a porosity distribution throughout the entire study area. Kriging was used as interpolation method because it assumes that the distance or direction between sample points reflects a spatial correlation that can be used to explain variation in the surface. With the

kriging method, the weights are based not only on the distance between the measured points and the prediction location but also on the overall spatial arrangement of the measured points.

2.1.3 Hydraulic conductivity

The hydraulic conductivity was determined at 16 locations where the groundwater exfiltrated from the channel bed and was converted to surface water. Those locations were detected by the addition of a small amount of uranine dye tracer in a shallow pit. At the location where the dye tracer emerged from the bed, an electrical conductivity (EC) meter was placed. A strong solution of water and salt was instantaneously poured into the pit while at the same time a stopwatch was started. Every ten seconds the EC was recorded. The measurement was stopped when EC reached its initial value. The EC were standardised by subtracting the initial value from the measured EC values.

The groundwater head gradient consists of the fraction of the difference in hydraulic head (dh; m) and the difference in distance between the pit and the location of exfiltration (dx; m). Therefore the shortest distance was measured with a tape measure and the difference in hydraulic head using a transparent tube and ruler. Subsequently breakthrough curves were made to determine the effective flow velocity [v_e; m/d] and specific discharge [q; m/d]:

$$q = v_e * n \quad (4)$$

The effective flow velocity was determined by dividing the distance by the time it had taken for 50% of the salt particles to flow through the soil. With the specific discharge, the hydraulic conductivity [K; m/day] was determined by Darcy's law:

$$K = | q/(dh/dx) | \quad (5)$$

2.1.4 Discharge

The quantity of hyporheic exchange between surface water and groundwater was determined by the solution of a known amount of uranine dye into the river. The experiment was carried out twice for which known quantities of uranine, 30 gram and 60 gram, were released instantaneously upstream of the research area. Downstream of the research area (880 m), the

concentration development was measured using a fluorimeter. During the experiments the concentration development of a small amount of dissolved uranine was monitored in a bucket of water to determine the degradation of uranine due to the influence of sunlight. Due to the degradation of uranine by sunlight a correction in the concentration development had to be done.

2.1.5 Resistivity

Resistivity measurements were carried out in order to determine the depth of the water carrying layer. The water carrying layer started at the groundwater depth and was bounded by the bedrock at the bottom. Resistivity measurements were carried out with the Abem Terrameter Signal Averaging System 300C (Abem SAS 300C). With this instrument electrical surveys were done and the subsurface resistivity distribution was determined. The values of the surface electrical resistivity measurements depended on the electrical resistivities and distribution of the surrounding soil, water and rocks. The resistivity was affected by various parameters: porosity, water content, mineral content, metal content, salinity of the pore water and grain size distribution (USEPA electrical methods).

To interpret the measurement data it was assumed that the subsurface consisted of horizontal layers whereby the apparent resistivity changed only with depth, but not horizontally. The amount of pore space controlled the absorption of the electric waves. The measured signal was a measure for the determination of the soil type.

The used electrical array for this research was the 4-electrode Schlumberger configuration with Vertical Electrical Sounding (figure 2.1). The distance between the two (inner) potential electrodes α (m) remained fixed while the (outer) current electrodes were moved outwards. The distance between the measurement device and a current electrode was called s (m). The spacing α was never allowed to be larger than 0.4*s equation 6 was not valid. When the distance between the potential electrodes did not exceed 0.4*s, errors were between 2-3% (USEPA electrical methods; Loke, 1999). Therefore the distance between the two potential electrodes was chosen to be 1m and the minimum value of s was equal to 3 m. The electrodes were placed on metal pins which were placed into the soil at an interval of 0.5 m until a distance of 10 m.

The apparent resistivity (ρ_a; Ωm) of the subsurface could be calculated from these measurements (Loke, 1999):

$$\rho_a = \pi * \alpha \left[\left(\frac{s}{\alpha}\right)^2 - \frac{1}{4}\right]\frac{V}{I} \quad (6)$$

Where V (mV) is the voltage which could be read from the Abem SAS 300C and I (mA) is the current which was set to 5 mA. Since the fraction of voltage over current is equal to resistance [R; Ω], equation 6 can also be written as:

$$\rho_a = \pi * \alpha \left[\left(\frac{s}{\alpha}\right)^2 - \frac{1}{4}\right] R \quad (7)$$

The resistance could be directly read from the Abem SAS 300C.

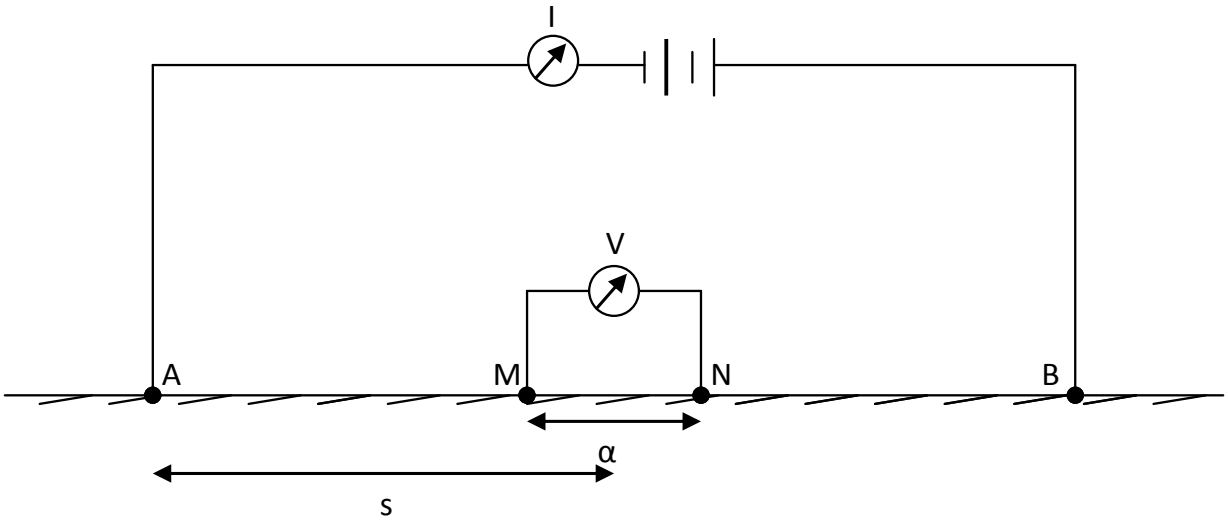

Figure 2.1: Schematic representation of the working of the Abem SAS 300C. This is the 4-electrode Schlumberger configuration. Adapted from Loke (1999).

2.1.6 Digital Elevation Model

An accurate digital elevation model (DEM) was necessary for modeling hyporheic exchange. Therefore two methods were combined to achieve the DEM: aerial photographs and differential global positioning system (dGPS) measurements. The coordinate system used for this study was WGS 84 (UTM).

The dGPS method used a local reference station of which the GPS coordinates were known and another base station receiver which was used to make position measurements. The base station receiver calculated its position based on satellite signals and compared this to the local reference station. The inaccuracy was applied to the data recorded by the base station receiver and corrected. Since the dGPS had an accuracy up to a couple of centimetres it was a good method for making a digital elevation model. More than 3500 dGPS measurements were done for e.g. water lines, old streams, reference points and notable height differences in the research area. Appendix E shows the locations of the dGPS measurement points.

Several aerial photographs of the research area were taken with a manually controlled airplane. This airplane was made of styrofoam and was equipped with a small camera which had a global positioning system connection, therefore every taken photograph had known coordinate points. The separate aerial photographs were combined to one orthophoto with the use of the computer program Photoscan from Agisoft. Photoscan generated high resolution georeferenced orthophotos and a DEM with a vertical accuracy up to 5 cm.

The measured dGPS z-coordinates were given in the UTM coordinate system. With Microsoft excel, the measured x- and y-coordinates were converted to real coordinates with the use of known UTM coordinates of a reference point which was a geological nail. To these known dGPS points the z-coordinates of the orthophoto were added. Since the z-coordinates of the orthophoto had to be converted to UTM coordinates a regression analyse from the Analysis Toolpak of Microsoft excel was applied. The z-coordinates of the dGPS measurements were included as dependent (y-) variables while the x-, y-, and z-coordinates of the orthophoto (X_{dGPS}, Y_{dGPS}, Z_{orth}) were included as independent (x-) variables. The coefficient of determination was high (0.933) and the independent variables were significant, however the standard error was relatively large (0.24 m). The coefficients for the independent variables (b,c,d) as well as the intercept (a) were calculated with the regression analyse. Now the z-coordinates ($Z_{prediction}$) of the orthophoto could be converted to UTM coordinates:

$$Z_{prediction} = a + b*X_{dGPS} + c*Y_{dGPS} + d*Z_{orth} \quad (8)$$

$$= 288437.1345 + 0.0267*X_{dGPS} + 0.0545*Y_{dGPS} + 0.6147*Z_{orth}$$

To determine whether the prediction was accurate, the regression residual was calculated by subtracting the z-coordinates of the orthophoto from the measured dGPS z-coordinates ($Z_{measured}$):

$$\varepsilon = Z_{measured} - Z_{prediction} \quad (9)$$

The coordinate points of $Z_{prediction}$ and the regression residual were added in separate layers to ArcMap. The regression residuals were interpolated with kriging whereby a layer with the interpolated error was made. Also the predicted z-coordinates were interpolated with kriging. The final DEM was made by summing the z-coordinates of the both layers.

2.2 Groundwater modeling

Modeling of hyporheic flow allows flexibility of the parameters and is a good method to investigate processes (Packman and Bencala,, 2000). Therefore, the finite difference code Modflow (McDonald and Harbaugh, 1996) was used for flow modeling, Water Budget for the calculation of fluxes (Harbaugh, 1990), and PmPath for forward particle tracking (Pollock, 1994). The program ArcGIS was used for the visualisation of the data.

2.2.1 Modflow models

Groundwater modeling was done with Modflow. First, a steady state model was made to create initial conditions, which could be used for the transient model.

The Modflow model viewing window had an extent of 314.9 m in the y-direction and 241.5 in the x-direction, which resulted in 315 rows and 241 columns. For this model cell sizes of one cubic meter were used, which resulted in a model that was accurate enough since field observations were also done on this scale. The steady state model had one unconfined layer (figure 2.2) which consisted of land, river, and side-streams (figure 2.3). The number of layers was based on resistivity measurements. The results of resistivity measurements are described in section 3.1.5. At a depth of 4.5 m bedrock was reached whereby the layer was defined by a

thickness of 4.5 m. The surface elevation was determined by the digital elevation model (DEM), while the bottom elevation of the layer was represented by the DEM minus the layer thickness of 4.5 m. The bottom elevation was dependent on the river gradient and therefore dependent on the gradient of the DEM. The steady state model had only one layer since it was assumed that bedrock did not participate in hyporheic flow.

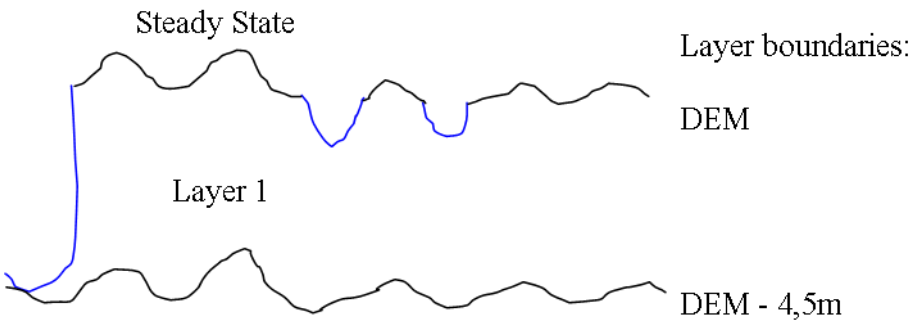

Figure 2.2: Schematic cross section of the steady state model.

With ArcGIS the hydraulic head and surface water level measurement points were interpolated using kriging to obtain the initial condition for the steady state calculations. Furthermore, observation points with known material sorting and a porosity value were added to ArcGIS. In order to get a distribution of porosity values of the area, interpolation with kriging was applied. The hydraulic conductivities were calibrated using the hydraulic head measurements by means of least squares fitting.

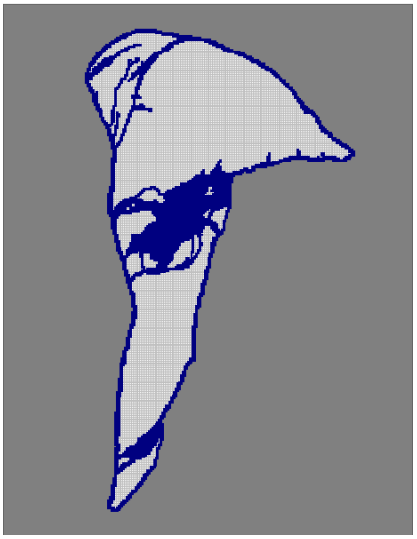

Figure 2.3: Cell status for the steady state model. Light grey is active; dark grey is inactive; blue is constant head.

Second, a transient model was made to simulate groundwater flow through time. The transient model area had the same extension as the steady state model. However the transient model had two layers instead of one single layer. The first (upper) layer was unconfined and had a thickness which basically depended on the hydraulic head of the groundwater (figure 2.4). The first layer had a large hydraulic conductivity in order to provide a fast discharge in case when the hydraulic head of the second layer would reach the first layer. With this transient model the dimensions of the river was able to vary. The bottom of the upper layer was equal to the top of the second layer. The top of the second layer was defined by the DEM. The thickness of the first layer was set to 5.5 whereby the whole model had a vertical thickness of 10 m. The second layer was set to unconfined/confined whereby the transmissivity varied. Conditions for the initial head were determined with steady state conditions for the first period.

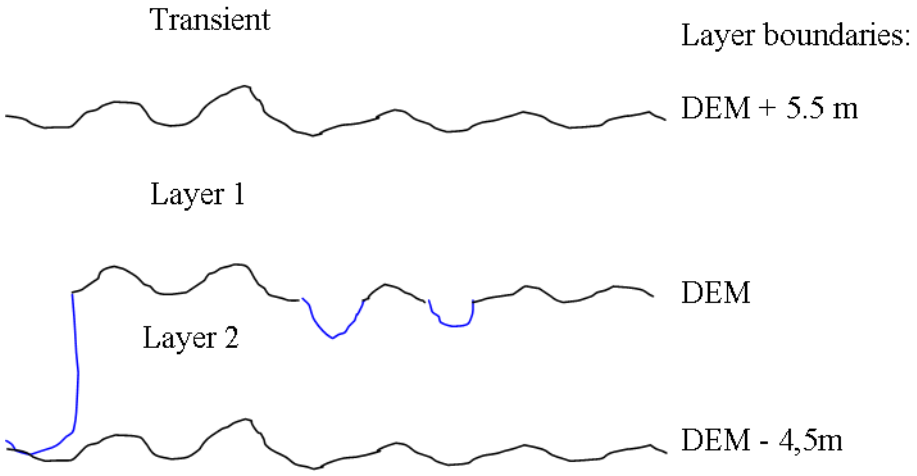

Figure 2.4: Schematic cross section of the transient model.

Layer 1 had cell status values based on the situation of only land (active cells) whereby the small streams which flowed through the research area were defined as land (figure 2.5). Layer 2 had a cell status division based on land and time-variant specified head (figure 2.6). The time variant specified head cells have a head value dependent on the water level for that period.

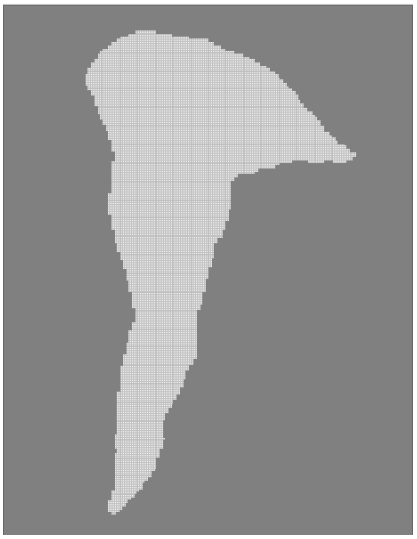

Figure 2.5: Cell status for layer 1 of the transient model. Light grey is active; dark grey is inactive.

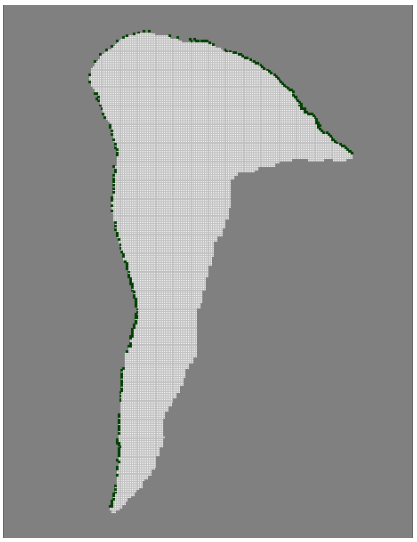

Figure 2.6: Cell status for layer 2 of the transient model. Light grey is active; dark grey is inactive; green is time variant specified head.

The transient model had 705 periods with a total length of 1080 days. Both layers had the initial hydraulic head distribution determined from the steady state model. To layer 1 a porosity value of 1 and a horizontal hydraulic conductivity value of 1 m/s were assigned because water needed to be easily discharged through this layer. Layer 2 had the same porosity and hydraulic conductivity values as for the steady state model.

2.2.2 Residence time distribution

It was not possible to obtain the Darcy flow for each individual cell using Modflow. However, the Darcy Flow tool of ArcGIS calculated the Darcy flow for each individual cell and determines whether there is infiltration or not. The Darcy Flow tool of ArcGIS modeled two-dimensional, vertically mixed, horizontal, and steady state flow where the head was independent of depth. This tool calculated the average fluid velocity on a cell-by-cell basis. For each cell, the aquifer flux was calculated through each of the four cell walls, where the head difference between the two adjacent cells and the average of the transmissivity were assumed to be isotropic (uniform in all orientations).

In order to determine the groundwater volume balance, the groundwater discharge through the cell walls were calculated. The discharge [Q; m3/d] was calculated from the aquifer flux and the width of the cell wall [Δy; m]:

$$Q = U * \Delta y \quad (10)$$

The groundwater volume balance residual [R; m3/d] is the surplus or deficit of water in each cell given the net flow into the cell. For an ideal scenario, without in- or outflow, the groundwater volume balance residual should be zero for all cells. The Darcy flow tool in ArcGIS also calculated the flow field, which is a vector field of groundwater seepage flow velocities and gives both magnitude and direction.

The seepage flow direction and velocity of a particle within each cell is an indication for the cumulative residence time of that particle. Using PmPath the cumulative tracking time of particles could be calculated. PmPath is an advective transport model which retrieves the groundwater models from Modflow (Chiang and Kinzelbach, 1998). PmPath was used to calculate the groundwater paths and travel schemes by the semi-analytical particle tracking method. This method assumed that the density of the groundwater was constant and applied Darcy's law and the law of conservation of mass. More information about the methods used by PmPath for the determination of groundwater paths can be found in Chiang and Kinzelbach (1998).

The hyporheic flow residence times of water originating from the surface were determined through forward tracking using PmPath. For steady state modeling, in each cell along the river

and streams five particles were arranged as represented at figures 2.7 and 2.8. For transient modeling one particle was placed in the centre of 58 cells along the river. The reported residence times were the total time it took for a particle from infiltration into the hyporheic zone until seepage into surface water.

With the use of ArcGIS, cells at the boundary of land and surface water were selected. Cells which were responsible for infiltration were only selected when the flow direction was directly from surface water to land. The cell data of flow direction, flow velocity, and residence time were combined in order to determine the relation between groundwater residence times and flow velocity.

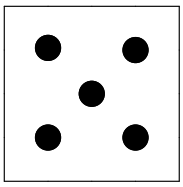

Figure 2.7: Particle distribution within a cell from above.

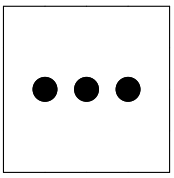

Figure 2.8: Particle distribution within a cell from side view.

Chapter 3 Results and Discussion

3.1 Fieldwork results

3.1.1 Hydraulic head

The hydraulic heads for both groundwater and surface water decreased linearly (figures 3.1 and 3.2). For further information, the groundwater and surface water level data are presented in appendix A. The locations of ground- and surface water level measurements at pits, monitoring wells, and metal pins are given in figure 3.3. Furthermore, this figure shows the interpolated hydraulic head distribution for 6 June 2013.

During the measured period the ground- and surface water levels decreased, which was similar to the decrease in river discharge. From 3 June 2013 until 19 June 2013 groundwater heads lowered by an average of 0.10 m. From 10 June 2013 to 19 June 2013 the surface water levels lowered by an average of 0.06 m (appendix A). The surface water levels decreased thus slower than groundwater heads. The week before the measurement period, the water level in the river decreased rapidly. As a result, the groundwater level has a lag and is thus decreases faster. In general, a decrease in the surface water level resulted in a decrease in groundwater levels throughout the area. Except for groundwater measurement points 3, 4, and 5 which had a total groundwater level lowering of 0.04 m. This lesser decrease could be the result of locations of the measurement points which was in an old gully. This gully becomes active for high river discharges. It was possible that the gully was able to transport subsurface flow from the side stream in the east towards the main river channel in the west. The active subsurface flow under the gully could have led to a retained hydraulic head relative to other locations.

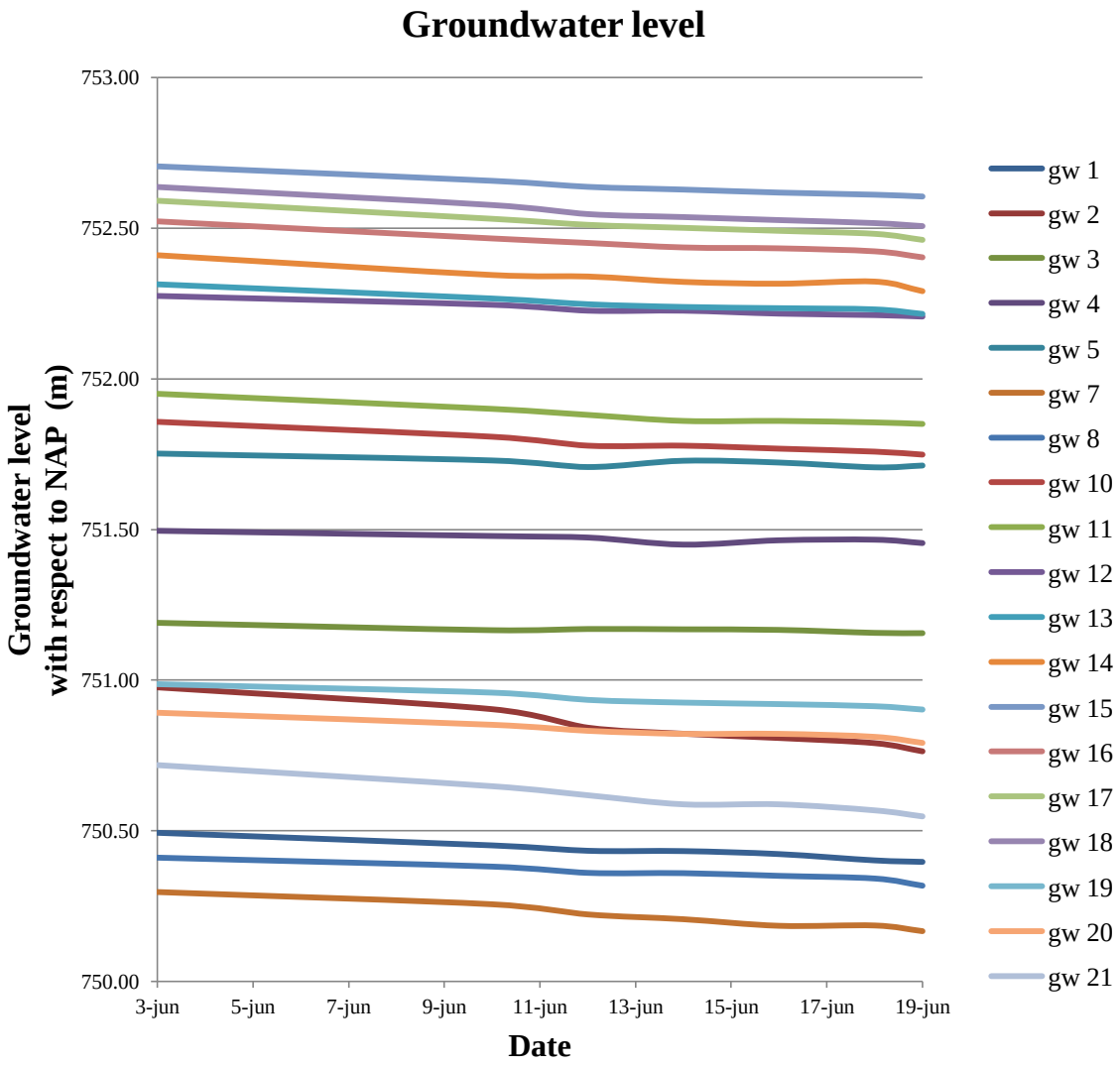

Figure 3.1: Groundwater level development from June 3 to June 19. In general, the decrease in groundwater is linear.

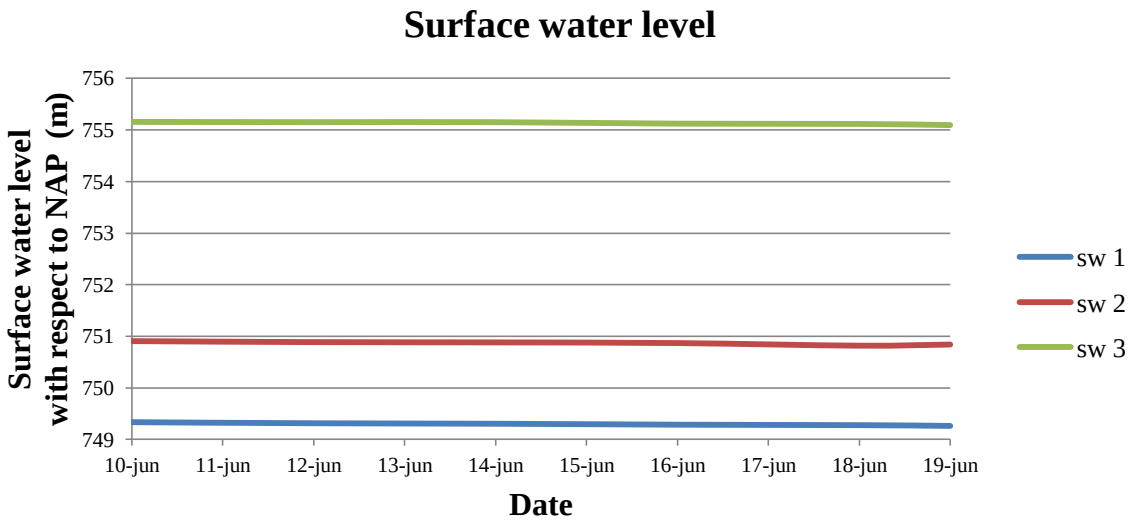

Figure 3.2: Surface water level development from June 10 to June 19. The decrease in surface water is linear.

The hydraulic head varied from 753.953 m in the north-east to 749.854 m in the south-west (figure 3.3).

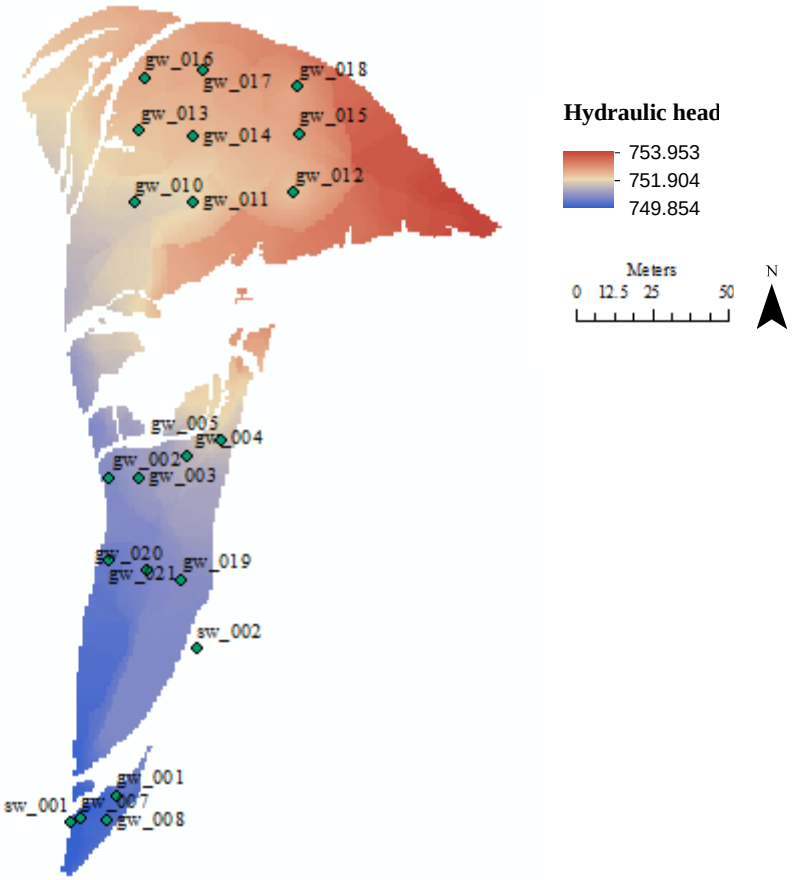

Figure 3.3: Interpolated hydraulic heads for 6 June 2013. This includes groundwater, surface water, and dGPS measurements. Furthermore, the groundwater and surface water measurement locations are given.

3.1.2 Porosity

The resulted porosity map is given in figure 3.4. The smallest porosities with a value of 0.18 were found in the vicinity of small streams in the centre of the map. The large porosity values in the north-west could be explained by the very good sorting of grains with almost no sand. The large porosity values at the north-east and south-east were a result of a mixture of good sorting and large boulders with a small portion of sand between them. The smallest porosities with a value of 0.18 were found in the vicinity of small streams in the centre of the map were the soil was sandy.

The sorting of the material and resulting porosity values were determined from surface observations. However, as was observed from locations where the river had incised the point bar, the sorting and porosity changed with depth. Furthermore, the porosity would decreased with depth as a result of compaction and the infiltration of fine sediments. The consequences due to compaction and infiltration of fine sediments could had an effect on the residence times of water and solutes in the hyporheic zone. However, this was not taken into account for modeling.

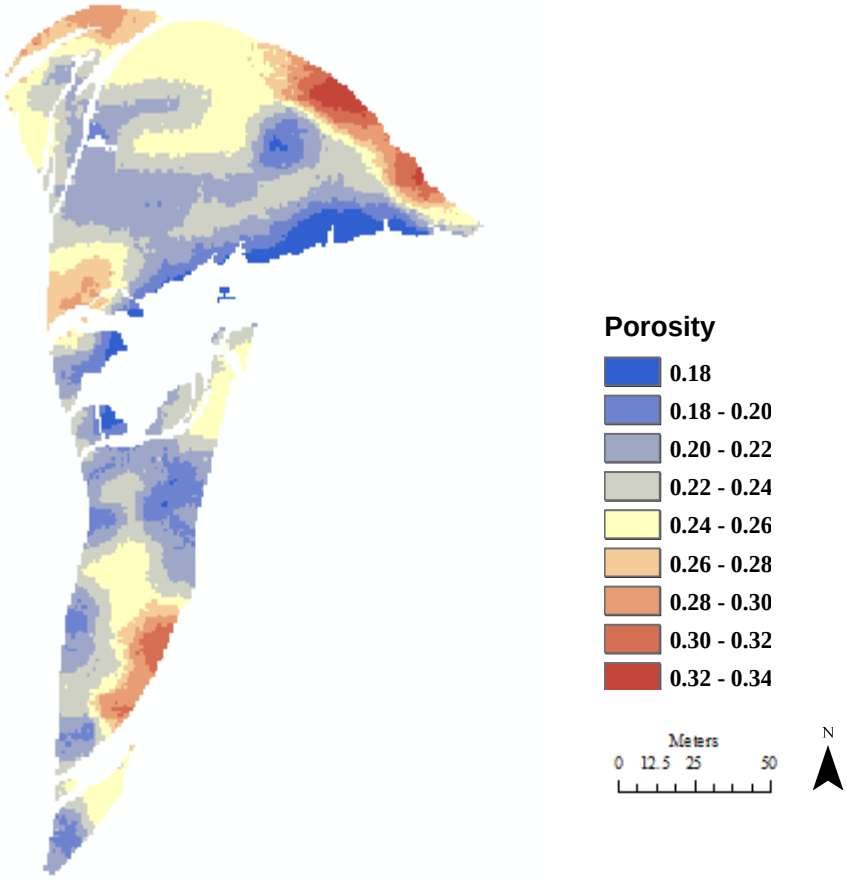

Figure 3.4: Map of the porosity distribution.

3.1.3 Hydraulic conductivity

Figure 3.5 gives an example breakthrough curve for salt experiment 1. All standardised alt tracer experiment breakthrough curves are given in appendix B.

The standardised EC value increased rapidly and then gradually decreased. Since the EC is a measure for the salt concentration the same pattern will be obtained for other conservative solutes. Solutes travelling through the point bar may initially be flushed out rapidly but they leave behind a lasting low-level tail (Cardenas, 2008). The time to breakthrough was determined by calculating the time at which 50% of the salt tracer has passed the measurement location (figure 3.5).

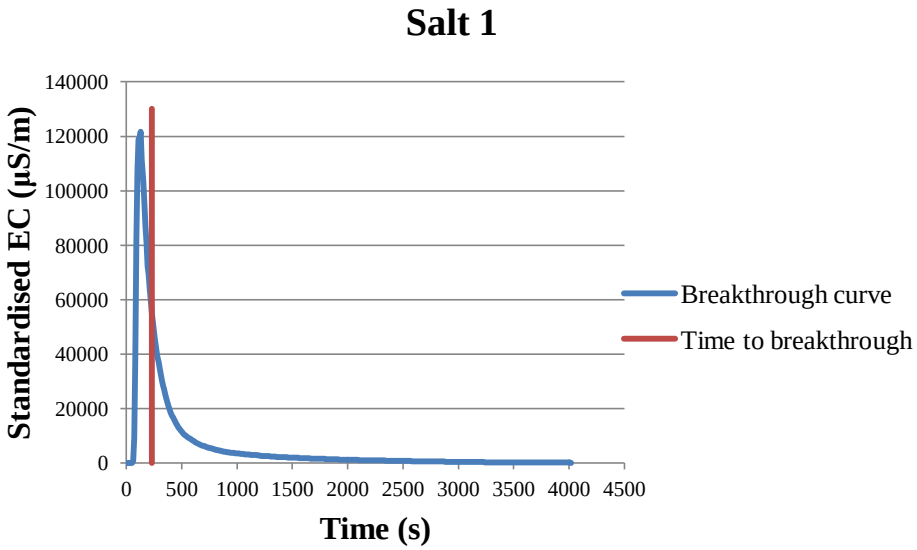

Figure 3.5: Breakthrough curve for salt experiment 1. The red line gives the time to breakthrough.

The calculated hydraulic conductivity values are given in table 3.1. Values range from 0.001 m/s to 0.285 m/s with an average value of 0.082 m/s. Figure 3.6 shows the measurement locations for the salt tracer experiments.

All determined hydraulic conductivity values fall within the ranges of gravel and sand, which is in accordance with field observations. Typical ranges for hydraulic conductivity values are: gravel from 10^{-3} to 1 m/s; clean sand from 10^{-6} to 10^{-2} m/s; clay from 10^{-12} to 10^{-8} m/s (Freeze and Cherry, 1979). Almost all experiments were done at locations situated at the interface of

surface and subsurface water (figure 3.6). The hydraulic conductivity also depended on packing and orientation of particles, which could have been different for locations more inland (Tonina, 2005). As a result of the inhomogeneity of the point bar, locations more inland might have had a smaller hydraulic conductivity value.

Table 3.1: Hydraulic conductivity values for salt tracer experiments.

Experiment	Hydraulic conductivity	
	(m/s)	(m/d)
1	0.046	3932.381
2	0.222	19150.565
3	0.053	4539.346
4	0.279	24085.633
5	0.262	22659.135
6	0.007	638.926
7	0.285	24612.642
8	0.027	2296.804
9	0.012	1017.815
10	0.016	1420.643
11	0.009	772.607
13	0.003	280.132
14	0.001	96.857
15	0.009	740.483
16	0.003	291.211
Average	0.082	7102.345

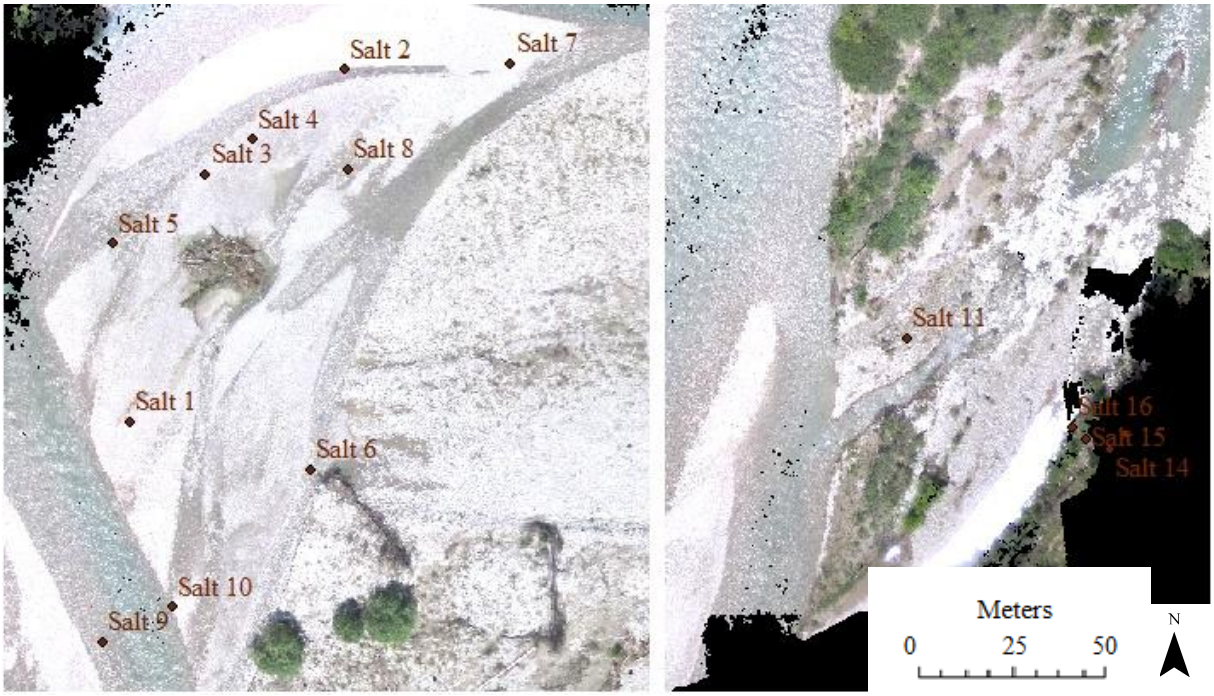

Figure 3.6: Measurement locations for hydraulic conductivity determination. Left: north-west of study area. Right: south of study area.

3.1.4 Discharge

Three additional experiments were carried out to determine the degradation rate of uranine under the influence of sunlight. A trendline was drawn through the graph of the logarithmic of the concentration [C; g/L] versus time [t; s]. From this trendline the slope [k; g/mL/s] was determined (table 3.2). Since the trendline was in the form:

$$\text{Log } C = k * t + \log C_0 \quad (11)$$

The corrected concentrations [C_{corr}; g/L] were determined by:

$$C_{corr} = C / 10^{k * t} = C / 10^{-0.00008 * t} \quad (12)$$

Whereby the slope was the mean from the three total curves. However, the slope would have been different when the weather conditions were taken into account (table 3.2). Sunny and little cloudy weather conditions would have resulted in a steeper slope of -0.00014 1/s and -0.00011 1/s, respectively. Cloudy weather conditions would have resulted in a less steep slope of -0.00006 1/s. Therefore, more sunny weather conditions results in a faster degradation of uranine and lower concentration values. Figures 3.7 and 3.8 show the concentration

developments for the uranine experiments for both the measured and corrected concentrations.

Table 3.2: Graph slope values for different weather conditions.

Bucket experiment	Weather conditions	Slope (1/s)
1	sunny	-0.00020
1	total curve	-0.00010
2	little cloudy	-0.00002
2	sunny	-0.00007
2	total curve	-0.00005
3	little cloudy	-0.00020
3	cloudy	-0.00006
3	total curve	-0.00010
	Mean slope total curves	-0.00008
	Mean slope sunny conditions	-0.00014
	Mean slope little cloudy conditions	-0.00011
	Mean slope cloudy conditions	-0.00006

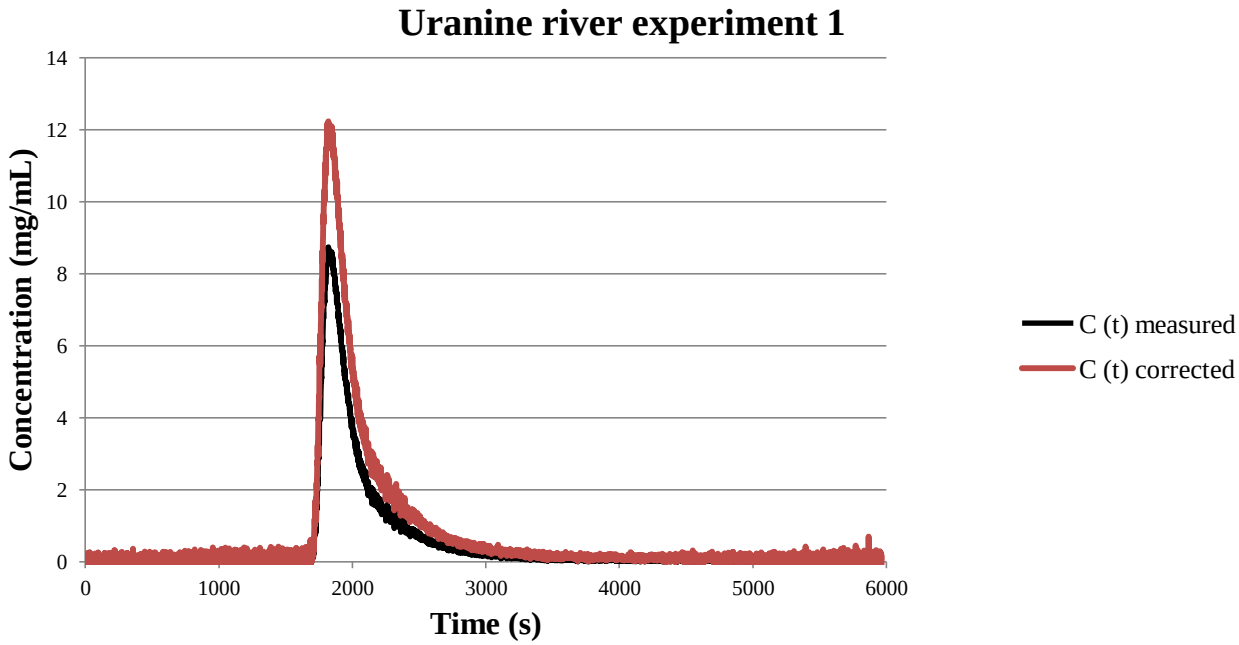

Figure 3.7: Concentration development uranine river experiment 1. The measured concentrations are smaller than for the corrected concentrations for the sun's influence on the concentration decrease.

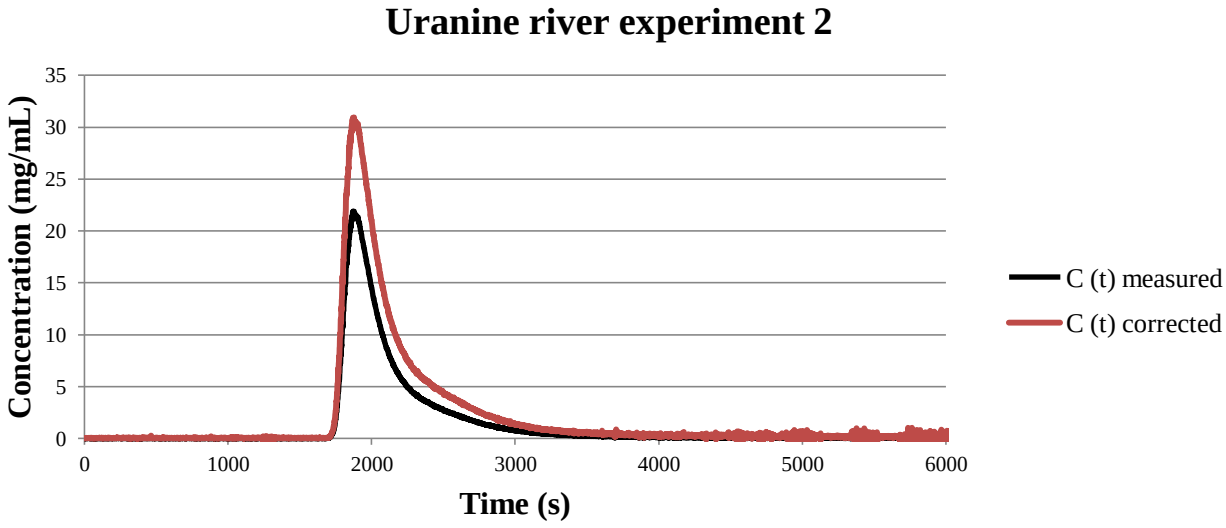

Figure 3.8: Concentration development uranine river experiment 2. The measured concentrations are smaller than for the corrected concentrations for the sun's influence on the concentration decreased.

The flow velocity and discharge of the river was determined using the corrected concentration developments (table 3.3). During experiment 1 the river had a flow velocity of 0.449 m/s and during experiment 2 the river had a flow velocity of 0.434 m/s. The flow velocity curve for La Roche des Arnauds (situated 25 km upstream) during the fieldwork period is given in appendix C.

The river discharges were determined with average concentrations. The discharge was determined by dividing the total mass of uranine [M; g] by the average measured concentration [$C_{average}$; m^3/d] which was multiplied by the total measuring time [t_m; d]:

$$Q = \frac{M}{C_{average} * t_m} \quad (13)$$

The discharge of the first experiment was equal to 601840 m^3/d (6.966 m^3/s). The discharge of the second experiment smaller: 409973 m^3/d (4.745 m^3/s).

The discharge was less at the second experiment than at the first experiment. Note that the first experiment was done on June 12, 2013 while the second experiment was done 8 days later, on June 20. The decrease in discharge was due to the decrease in precipitation and melt water transported by the Petit Buëch river.

The above calculation of discharge assumes that 100% of the released uranine tracer passed the downstream measurement location. However, a small proportion of the uranine tracer could have been lost by infiltration to the hyporheic zone, which could lead to a slight underestimation of the discharge.

Table 3.3: River flow velocities and discharges on 12/6/2013 (experiment 1) and on 20/6/2013 (experiment 2). The discharges are determined with the average concentrations.

		Experiment 1	Experiment 2
Mass uranine	(g)	30	60
Measuring time	(d)	0.069	0.071
Distance (thalweg)	(m)	880	880
Flow velocity	(m/s)	0.449	0.434
	(m/d)	38794	37498
Average concentration	(g/m3)	0.00072	0.00207
Discharge	(m3/s)	6.966	4.745
	(m3/d)	601840	409973

3.1.5 Resistivity

The apparent resistivity curves have a straight line for small electrode spacings between electrode spacings of 3.0 and 4.5 m (figure 3.9). The second part of the curves have a linear trendline. The intersect of the asymptote and the linear trendline gives the transition depth between two different layers, where the bottom layer represents bedrock. The straight line acts as an asymptote and represents the apparent resistivity for the surface layer (Telford et al., 1990). The value of the apparent resistivity was estimated by calculating the average. Between electrode spacings 3.0 to 4.5 m the apparent resistivity for the first field test was equal to 64.56 Ωm, and for the second field test 76.13 Ωm. The bedrock was reached at a depth of 4.5 m for both field experiments (figure 3.9).

The resistivity of the bedrock can be determined when there is a second asymptote visible for larger electrode spacing. Since there is no second asymptote present, this could not be determined. However, the maximum value of apparent resistivity for the bedrock was equal to 43 Ωm for both field tests. A table with the apparent resistivity values in combination with electrode spacings is given in appendix D.

The surface layer consisted of mainly limestones, pebbles and gravels with small proportions of clay as matrix. Limestone have a resistivity range of 50 to 10^7 Ωm while clays have a resistivity of 1 to 100 Ωm and soil water has a resistivity of approximately 100 Ωm (Telford et al., 1990). This is in agreement with the found apparent resistivities of 64.56 and 76.13 Ωm.

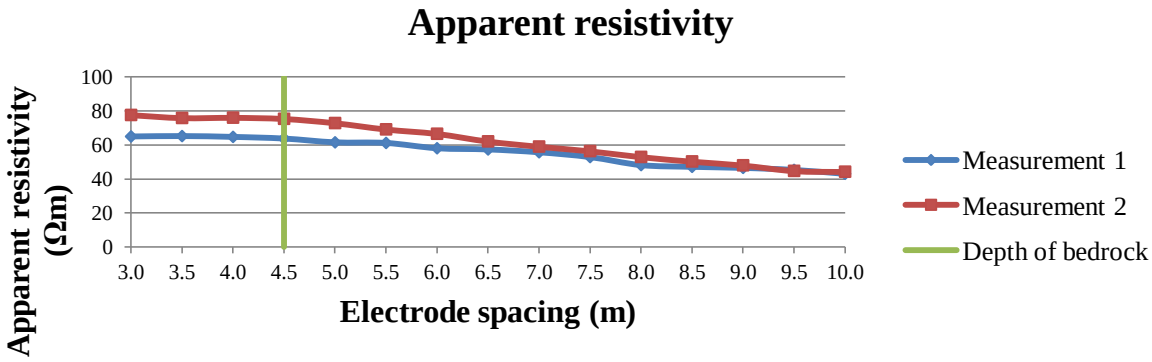

Figure 3.9: Graphs of the two apparent resistivity measurements. The green line indicates the depth of bedrock.

3.1.6 Digital elevation model

Surface elevations of the study area varied from 750.220 m to 754.384 m above mean sea level (figure 3.10). In general, the surface elevation decreased from north to south and from east to west, which was in agreement with the river gradient. The digital elevation model is a correct representation of reality as will be explained below.

Section A was submerged for a long time during the fieldwork. The low surface elevations which stretch from west to east at section B were in reality an old gully and the areas north and south of section B therefore had a relatively high surface elevation. Section B would become submerged during high river discharges. The land in the vicinity of section C was situated at a location where two factors played an important role: low surface elevation and flooding by small side streams of the main river channel. Those streams had a course over land which results in flooding when the land has a small surface elevation. At section D an alternation of low and higher surface elevations can be seen, as was also observed in reality. These alternations were a result of large discharge events. During high river discharge side channels flooded the land where sedimentation and/or erosion occurred. Humps in the

landscape were a results of sedimentation in combination with retention of the soil by vegetation.

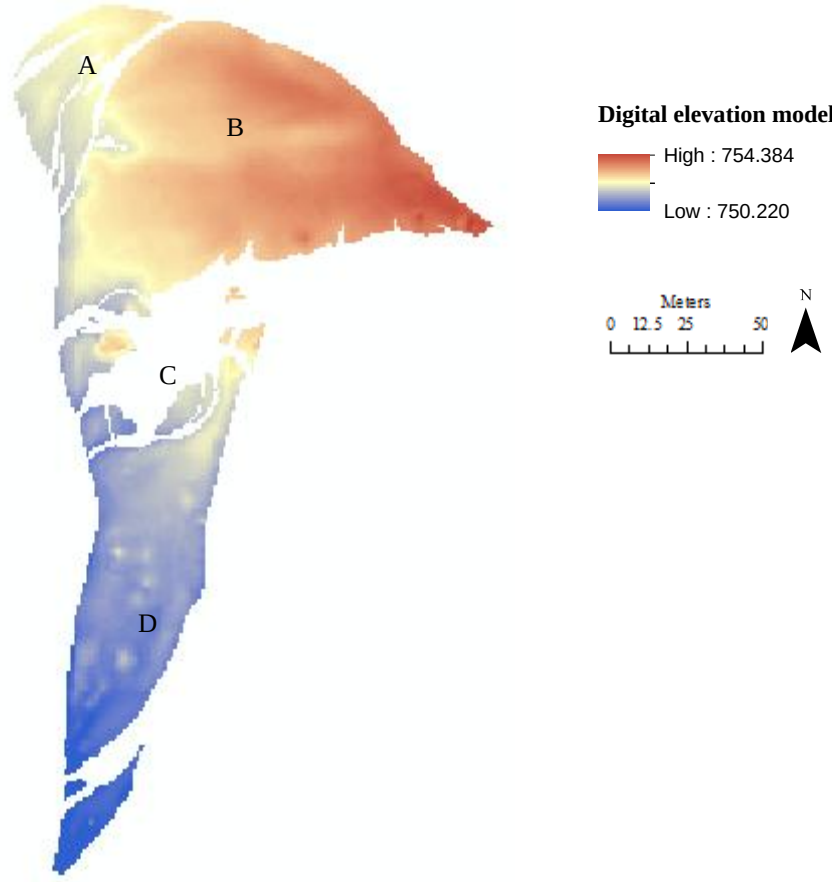

Figure 3.10: Digital elevation model of the study area. For this DEM 3500 dGPS points were used.

Since the DEM was made by summing of the interpolated, predicted, z-coordinates and the interpolated regression residuals, small deviations from reality could have occurred in the DEM. The regression residual for all data varied from -2.2 to 0.6 m. However, this was also for locations where no dGPS measurements were done. The regression residual distribution for only the locations where dGPS coordinates were known varied from -0.8 to 0.4, which was smaller and more accurate (figure 3.11).

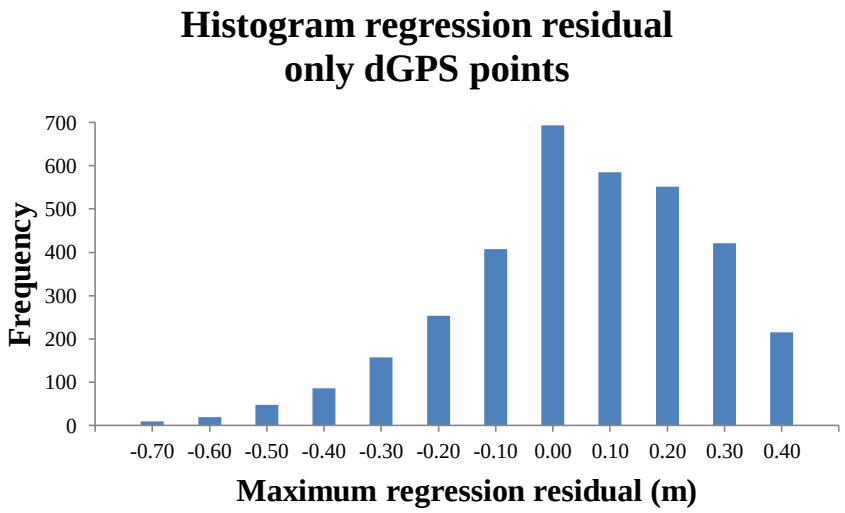

Figure 3.11: Histogram for the regression residual. The regression residual data for only the dGPS measurement points are given.

Figure 3.12 shows the map of the groundwater depth (difference between the DEM and the hydraulic head) for the study area. Most locations show water beneath the surface (groundwater) at a depth between 0 m and 1.40 m. A few locations show a water table at or above the surface (surface water) with a water depth between 0 m and 0.25 m.
Location A of figure 3.12 had a less deep groundwater depth (light red) relative to the surrounding area (dark red). In reality an gully remnant was located at A. Due to the lower surface elevation of the gully the groundwater depth was less. At location B and D a pool of surface water is indicated at the groundwater map. Those locations had a low surface elevation in combination with a high hydraulic head. The edges of the small side streams which submerge the point bar at location C had an alternation of positive and negative groundwater depths.

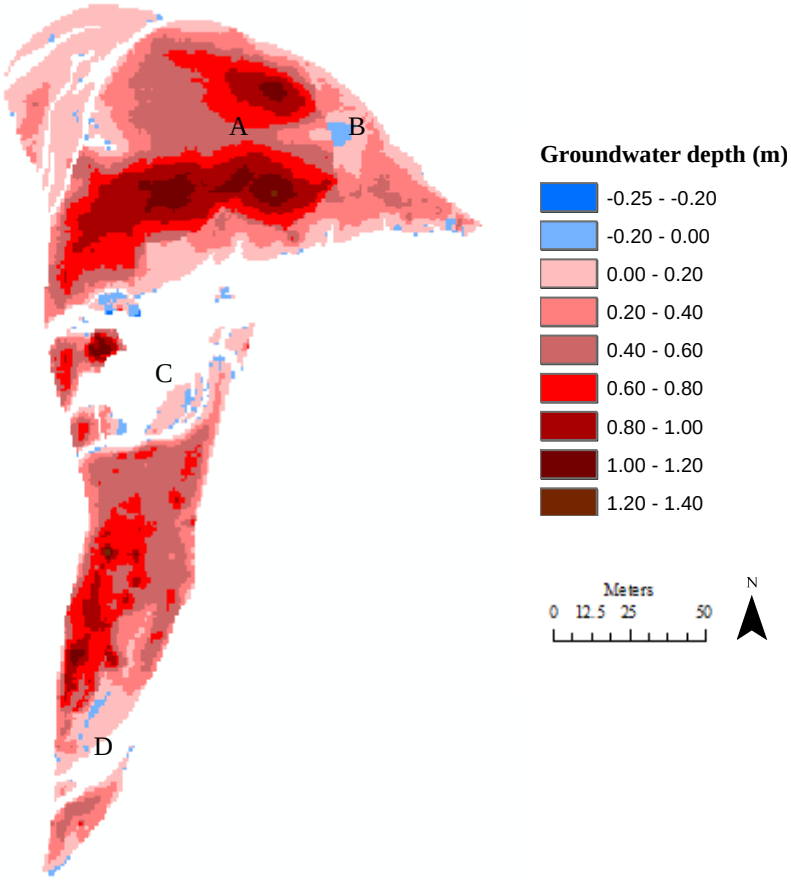

Figure 3.12: Figure of the groundwater depth in meters. Red colours indicate groundwater, blue colours indicate surface water.

3.2 Model results

3.2.1 Model calibration

The steady state model had to be calibrated for hydraulic conductivity in order to agree with the measured hydraulic head data. Therefore, different hydraulic conductivity values were compared to the hydraulic head data on two measurement dates. This was achieved using the least squares. The smallest sum square error was an indication for the calibrated hydraulic conductivity. The results were plotted on a log-log scale and a trendline was plotted through the results (figure 3.13). The minimum sum squared error for June 10, 2013 corresponded to a hydraulic conductivity value of 0.039 m/s. The minimum sum squared error for June 19, 2013 corresponded to a hydraulic conductivity value of 0.011 m/s. The average hydraulic conductivity was equal to 0.025 m/s. The measured hydraulic conductivities ranged from 0.001 m/s to 0.285 m/s with an average of 0.082m/s (table 3.1). The measured hydraulic conductivity values were obtained at locations close to the surface water and groundwater interface. Due to the inhomogeneity of the point bar, locations more inland might have had a smaller hydraulic conductivity value resulting in a smaller calibrated hydraulic conductivity.

The determined hydraulic conductivity value of 0.025 m/s is in agreement with values found in literature. Marsily (1986) found a hydraulic conductivity value of 10^{-1} m/s to 10^{-2} m/s for coarse gravel and 10^{-1} m/s to 10^{-5} m/s for a mixture of sand and gravel. Adams and Gelhar (1991) found a smaller hydraulic conductivity value of 10^{-5} m/s to 10^{-3} m/s for very heterogeneous sand and gravel. Hydraulic conductivity values for alluvial deposits varied from $3*10^{-4}$ m/s (Dieulin, 1980) to $1*10^{-3}$ m/s (Fried and Ungemach, 1971). Konikow and Bredehoeft (1974) found hydraulic conductivity values between $2.4*10^{-4}$ m/s and 4.2 10^{-3} m/s for alluvial deposits.

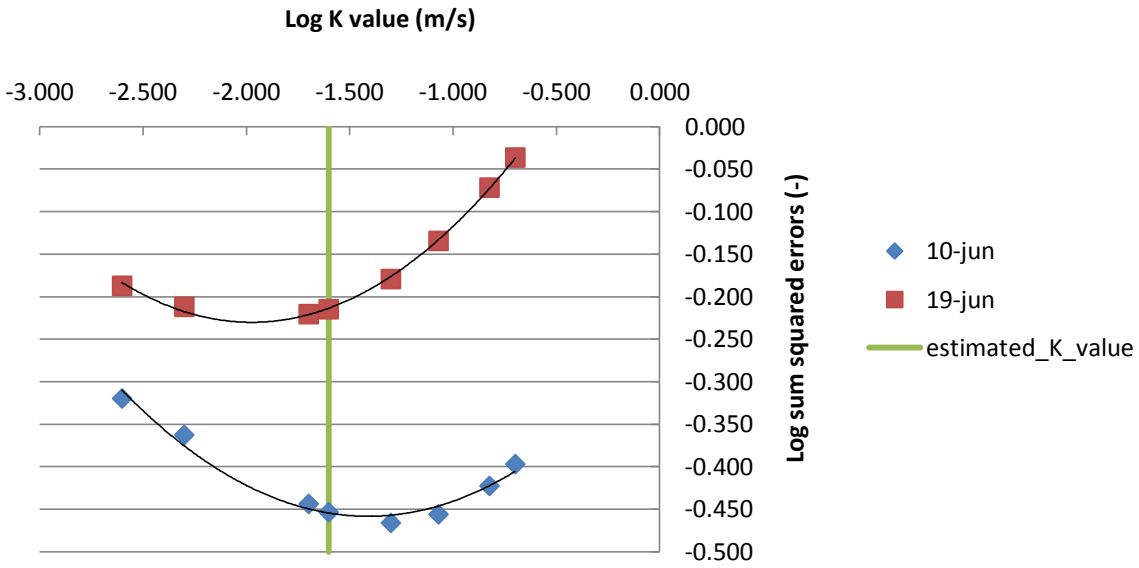

Figure 3.13: Results hydraulic conductivity calibration. The estimated hydraulic conductivity value is equal to 0.025 m/s.

For the steady state, a hydraulic conductivity of 0.025 m/s was used which resulted in small differences in modeled versus measured hydraulic heads. These errors are given in figures 3.14 and 3.16. The hydraulic head errors range from -0.6 m (overestimation of the model) to 0.012 m (underestimation) with a mean error of -0.059 m for June 10th and -0.182 m for June 19th. The distribution of the errors can be seen from the histograms (figures 3.15 and 3.17). Overall, most errors had a maximum of 10 cm.

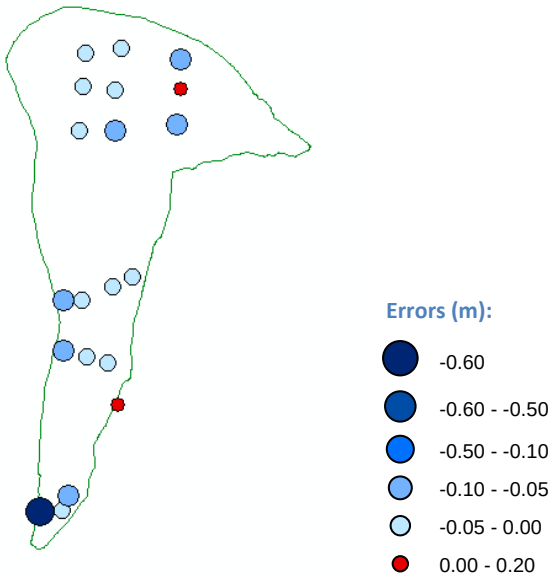

Figure 3.14: Hydraulic head errors June 10, 2013 for an hydraulic conductivity of 0.025 m/s. Negative values indicate an overestimation of the model.

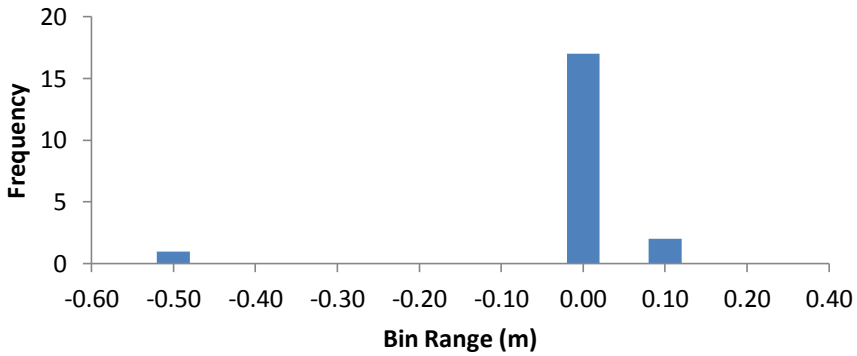

Figure 3.15: Histogram hydraulic head errors June 10, 2013.

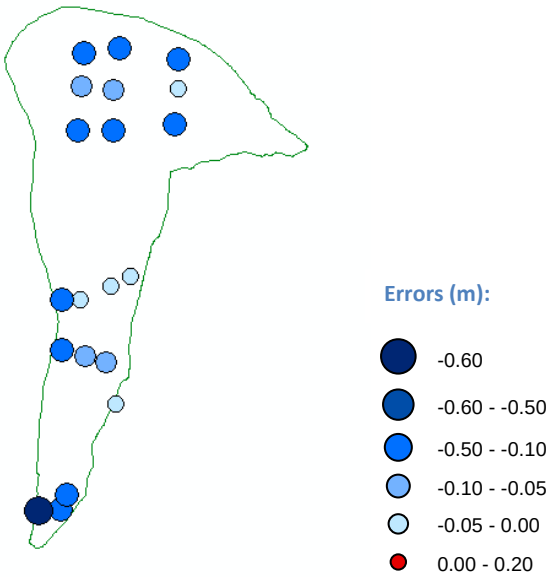

Figure 3.16: Hydraulic head errors June 19, 2013 for an hydraulic conductivity of 0.025 m/s. Negative values indicate an overestimation of the model.

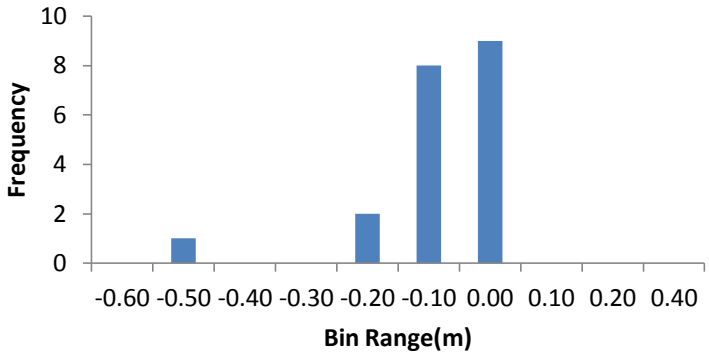

Figure 3.17: Histogram hydraulic head errors June 19, 2013.

The overestimation of the hydraulic heads was mostly close to the river. The reason for this is probably due to the larger hydraulic conductivity than on average. More inland locations could have a smaller hydraulic conductivity.

3.2.2 Steady state model calculations

At the interface of surface water and subsurface water infiltration from or exfiltration into the river occurred. Figure 3.18 shows a map of infiltration and effluent seepage rates at the interfaces of surface- and subsurface water for steady state conditions. Infiltration rates varied from 0.01 m/d to 0.10 m/d and effluent seepage rates varied from 0.01 m/d to 0.14 m/d. However, infiltration and exfiltration rates of more than 0.04 m/d were less common. Most infiltration occurred in the north-east and south-east of the point bar whereas most seepage into the river occurred in the west of the study area.

Hyporheic exchange was caused by head gradients and pressure differences. Head gradients were a result of streambed topography and water surface topography. The sediment of the point bar acted as an obstruction and caused high pressure on the river side and low pressure on the point bar side whereby water entered the point bar. Since infiltration of water and solutes occurred at high pressure zones, low pressure zones were dominated by effluent seepage (Wörman et al., 2002).

According to the Water Budget calculator of Modflow, the total amount of infiltration into the hyporheic zone was equal to 1.097 m^3/d and the total amount of seepage was equal to 1.098 m^3/d. Therefore, the net outflow was equal to -0.0008 m^3/d, or -0.774 L/d, which was nearly negligible. The Water Budget calculator determined a flux of $1.912*10^{-5}$ m^3/d from the surface down into the point bar, and a flux of $1.916*10^{-5}$ m^3/d moved from the point bar to the surface. This was a net flux of 0.0041 m^3/d towards the surface layer. The surface layer had a large hydraulic conductivity which resulted in a fast discharge of particles out of the hyporheic zone. The quantity of discharge via the surface was small, meaning that most flow in the hyporheic zone was seepage into side streams or directly in the Petit Buëch river.

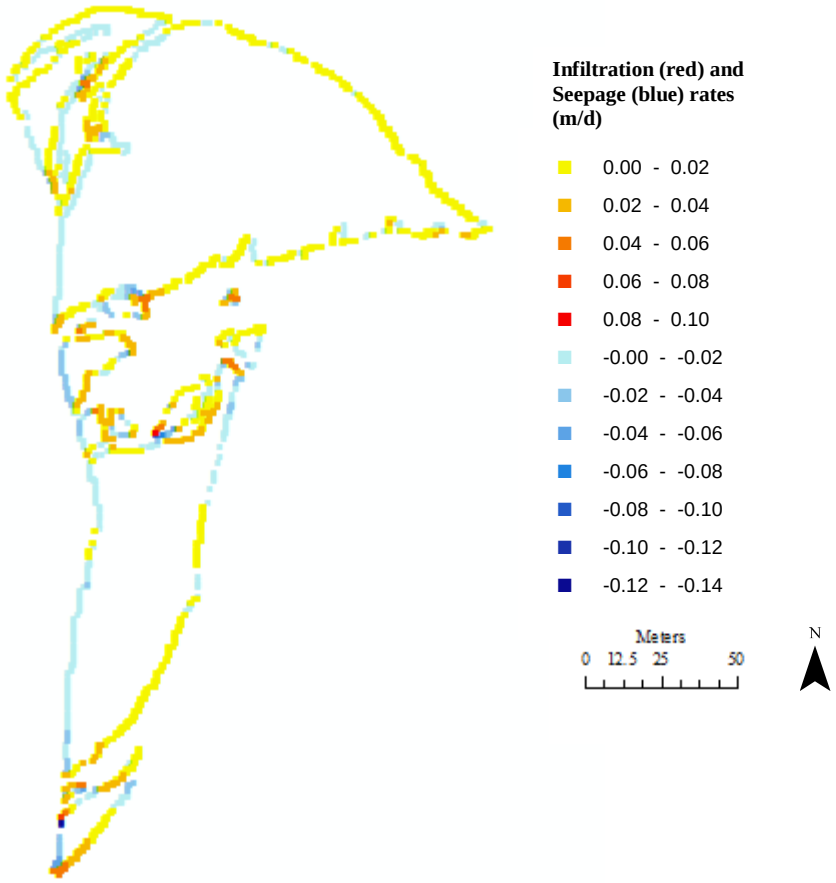

Figure 3.18: Infiltration and exfiltration rates.

The infiltrated surface water had a Darcy velocity which is displayed in figure 3.19. Largest Darcy velocities could be found at locations where side streams flooded the area as a consequence of the large flow velocity of the streams.

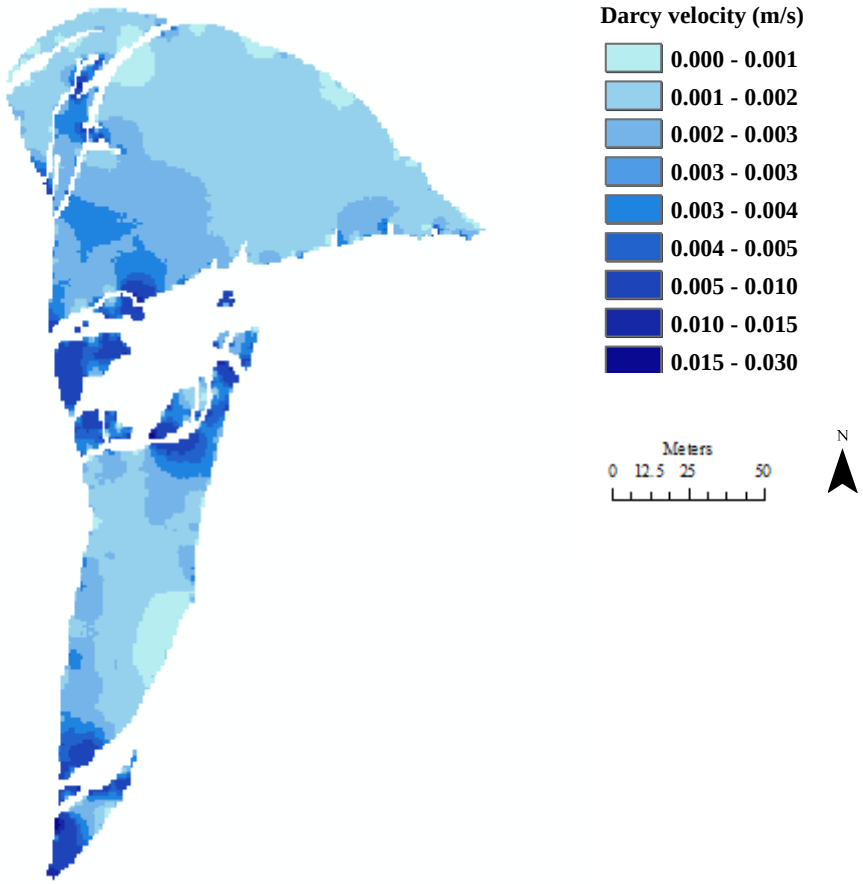

Figure 3.19: Darcy velocities distribution over the research area.

The frequency curve of the cell horizontal discharge which contributed to infiltration, increased from 0 to 0.006 m^3/d and decreases slowly to 0 for 0.09 m^3/d (figures 3.20 and 3.21). Almost 50% of the total discharge had a discharge of maximal 0.01 m^3/d. From this, about 30% had a discharge between 0.006 m^3/d and 0.008 m^3/d (figure 3.21).

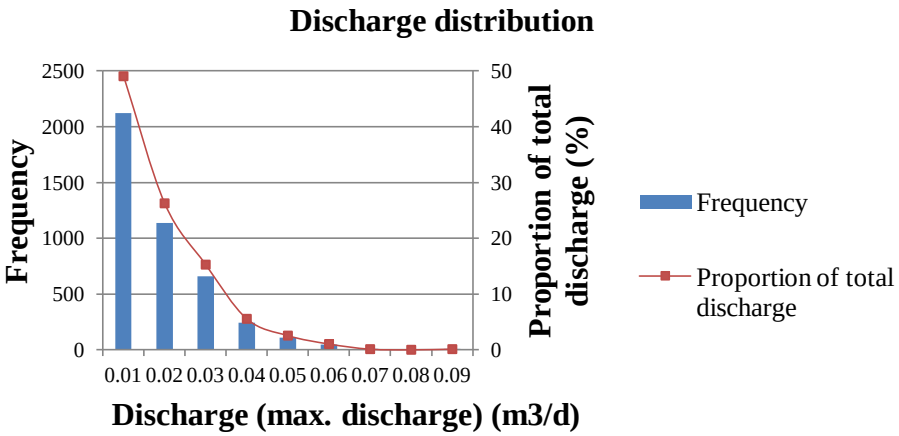

Figure 3.20: Histogram of the discharge distribution for the study area and graph of the proportion of total discharge.

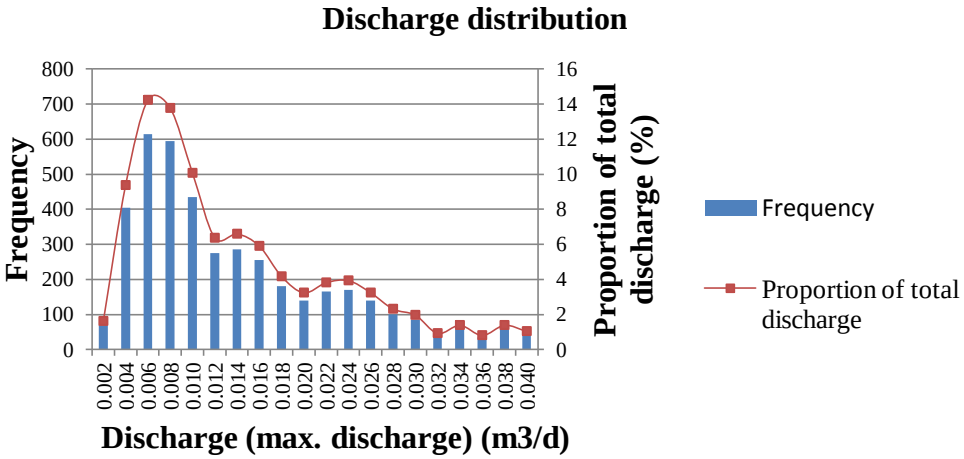

Figure 3.21: Histogram of the discharge distribution for the study area and graph of the proportion of total discharge. Both zoomed in for discharges of maximal 0.040 m^3/d.

The residence time distribution can be interpreted as the breakthrough of a tracer which was released over the study area with the assumption that the tracer was conservative and instantaneous released (Maloszewski and Zuber, 1982). The spatial distribution of residence times for the study area with the steady state conditions and river discharge occurring at June 12, 2013 is given in figure 3.22. Residence times varied from 5 hours to 857 days. The longest residence times were found in the north-east of the point bar. Relatively short residence times of maximal 100 days were found at the centre and south of the research area.

The long residence times in the north-east were a result of the flow direction after infiltration (figure 3.23). Water and solutes which entered the hyporheic zone travelled a long distance

before upwelling into surface water occurred. Figure 3.24 shows flow paths of infiltrated water and solutes in the south of the research area. The given particles and their flow paths had a long residence time (more than 100 days). Heterogeneity of the alluvium determines the location of downwelling and upwelling water (Cardenas et al., 2004). Upwelling occurs when the velocity of the subsurface flow reduces due to a reduction in hydraulic conductivity or when there is a low pressure zone. Downwelling occurres when the velocity of hyporheic flow increases due to, for example, the increase in hydraulic conductivity. Moreover, downwelling of surface water into the hyporheic zone occurres when there is a high pressure zone present (Tonina and Buffington, 2009).

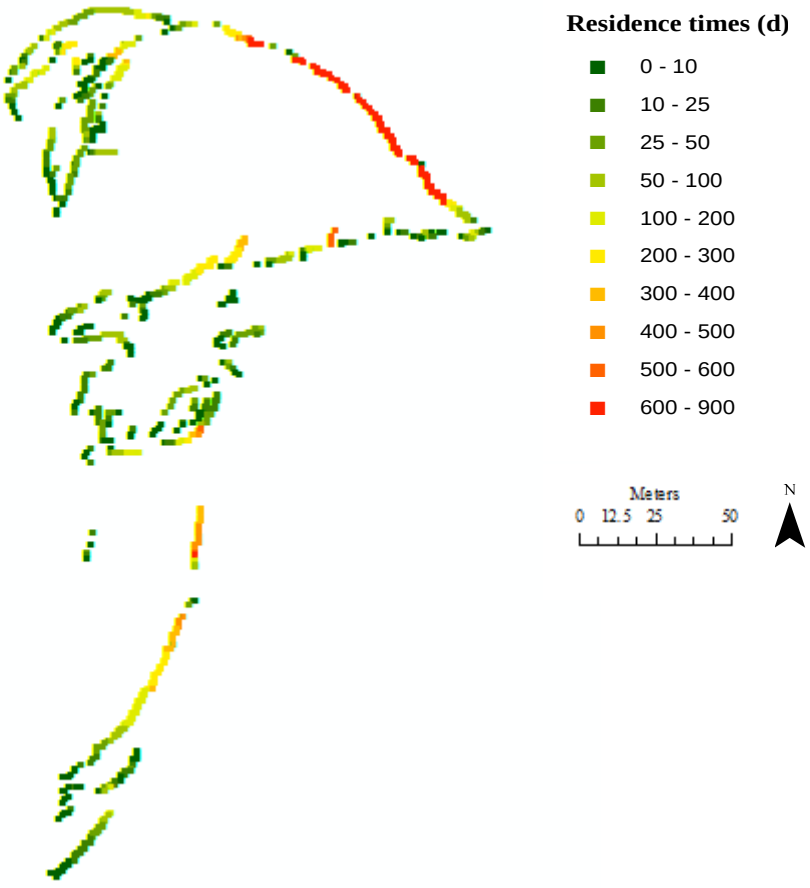

Figure 3.22: Map of the residence time distribution for the study area. The given residence time for each cell is the maximum of the five released particles.

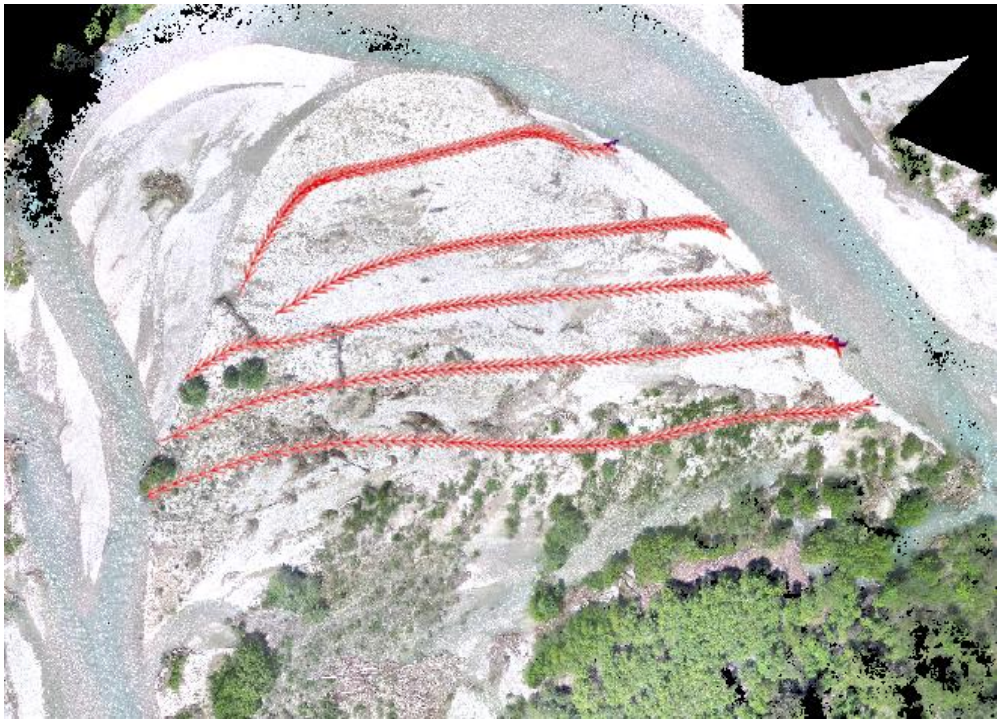

Figure 3.23: Flow paths of infiltrated water and solutes in the north-east. Every arrow represents a residence time of 10 days.

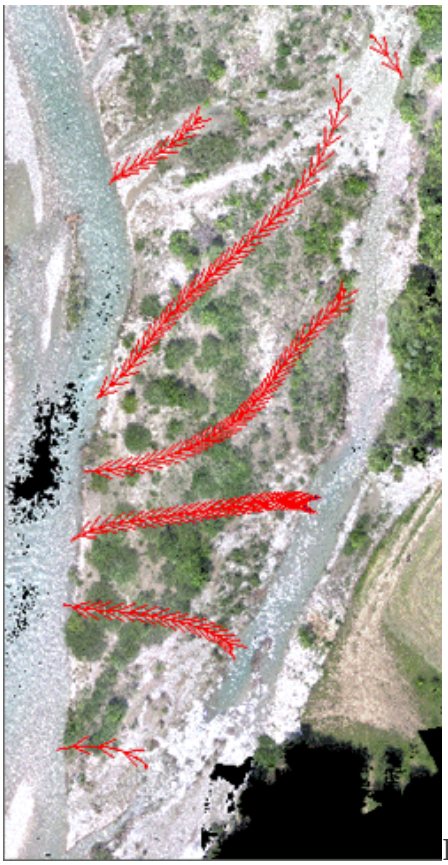

Figure 3.24: Flow paths of infiltrated water and solutes in the south. Every arrow represents a residence time of 10 days.

About 60% of the total residence times were between 0 and 50 days and 10% between 50 and 100 days (figure 3.25). The rest, approximately 30%, of the released particles had a residence time of more than 100 days. A small frequency peak was present between 600 and 850 days. Figure 3.26 has zoomed in for residence times between 0 and 150 days. The graph has a peak value of 27% for a maximum of 10 days and gradually declines to 150 days.

Most short residence times occurred in the centre of the area and were a result of side streams flowing through the area. Most flow paths started at a side stream before becoming subsurface flow for a short amount of time until exiting in one of the side streams again. Particles with long residence times of around 700 days originated from the north-east where also relatively much infiltration occurred. Those long residence times resulted in a frequency peak around 700 days. Particles that infiltrated at this location had a long travel time before exfiltrating into the river (figures 3.22 and 3.23).

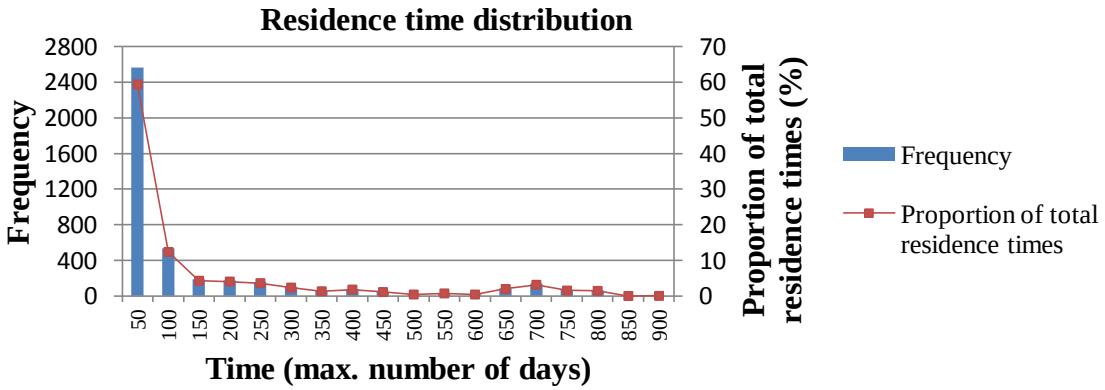

Figure 3.25: Frequency histogram of the residence time distribution for the study area and graph of the residence time distribution, given as the proportion of total residence times.

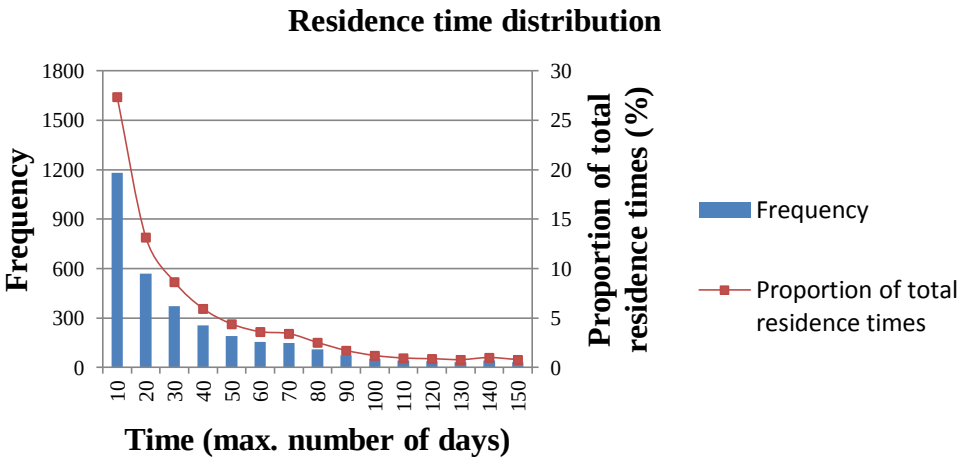

Figure 3.26: Histogram of the residence time distribution of the study area and graph of the residence time distribution, given as the proportion of total residence times. Both zoomed in for residence times of maximal 150 days.

The plot of hyporheic exchange rates [Q_{HE}; m^3/d] versus residence times [RT; d] implies that the hyporheic zone had a large range of residence times (Haggerty et al., 2002) (figure 3.27). This is an indication that the hyporheic zone contained a significant volume of water with a long residence time. As a result, the hyporheic zone could retain large quantities of solutes from stream water which may be released back into the stream after long residence times. Therefore, chemical signals due to e.g. precipitation, industrial pollution, or agriculture may be delayed or even attenuated by hyporheic zone exchange (Haggery et al., 2002).

In this case the relation between hyporheic exchange rates and residence times was:

$$Q_{HE} = 0.026 * RT^{-0.261} \quad (14)$$

The coefficient of determination was 0.375, which is quite low. This can be explained by the large variation in hyporheic infiltration rates and their related residence times due to the varying morphology throughout the study area. Changing porosities, surface elevations, and hydraulic heads resulted in the variation of streambed pressure gradients. Furthermore, the presence of small side streams and the Petit Buëch river altered the conditions of the point bar. As a result the hyporheic exchange rates and residence times varied along the interface between surface water and the hyporheic zone. In general, particles with a short residence time had a large hyporheic exchange rate whereas particles with long residence times had a small hyporheic exchange rate. However, it should be noted that re-infiltration of water and solutes into the hyporheic zone was not incorporated into the model. Since a small portion of

the total discharge infiltrated the point bar, re-infiltration will probably not be significant. Particles which exfiltrated from the hyporheic zone did not had the opportunity to infiltrate again. The plot of the hyporheic exchange rates versus residence times could have deviated from figure 3.27 when re-infiltration was incorporated.

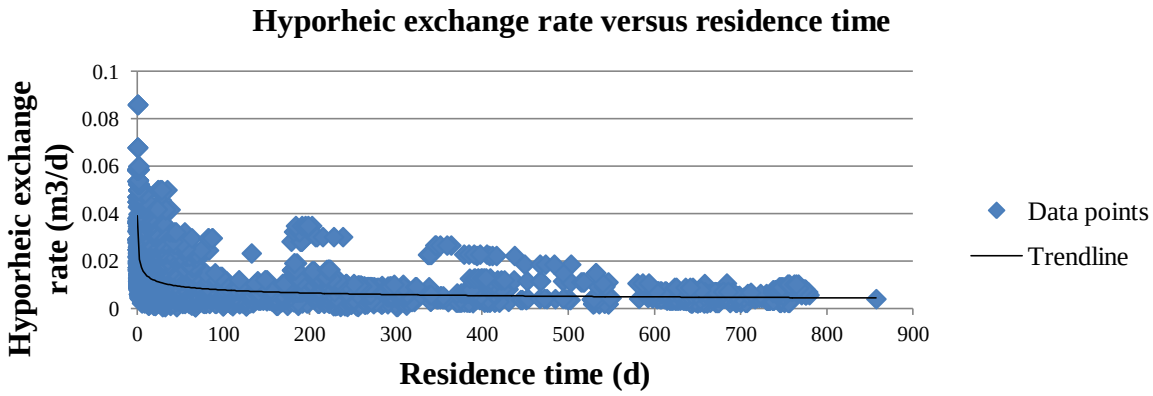

Figure 3.27: Graph of the hyporheic exchange rate plotted against residence time.

3.2.3 Transient model calculations

Figure 3.28 shows the average infiltration rates of the released particles for transient conditions. The average infiltration rate varied from 0.0014 m/d to 0.014 m/d. The largest infiltration rates occurred at the west side of the point bar while smaller infiltration rates mostly occurred at the north-east.

Since figure 3.28 only shows the average infiltration rates, this does not mean that there was only infiltration. Also seepage could have occurred at those locations. Figure 3.18, which represents the infiltration and seepage rates for steady state conditions, showed no infiltration on the west side of the point bar. The model of the steady state conditions used constant hydraulic head values and a constant water level. Therefore, particles were able to follow the gradient and migrated through the study area. Due to a gradient towards the west no particles were able to infiltrate at the western boundary of the point bar. With transient modeling the water level of the river fluctuated, resulting in a fluctuating hydraulic head and a variable gradient. As a result, infiltration and seepage locations varied through time.

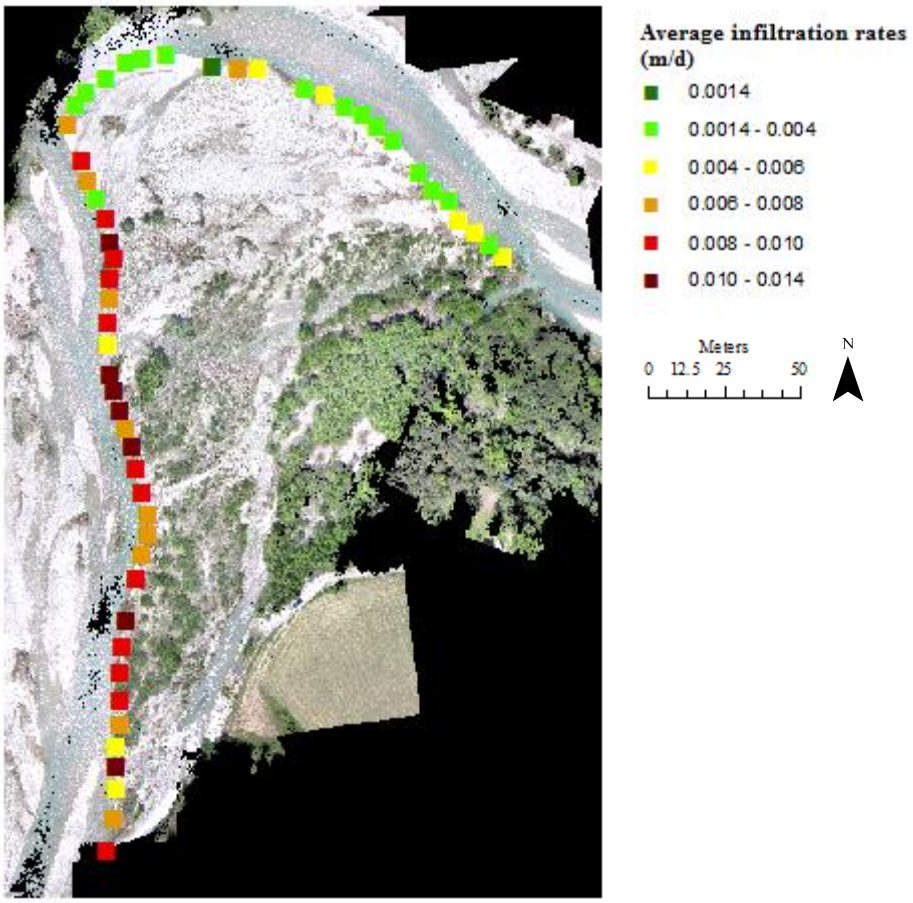

Figure 3.28: Average infiltration rates for transient conditions.

The frequency curve of the horizontal discharge into a cell increased from 0.001 m^3/d to 0.004 m^3/d and decreased gradually to 0.032 m^3/d (figure 3.29). Approximately 40% of the total discharge was between 0.002 m^3/d and 0.005 m^3/d. Almost 99% of the total discharge was between 0.001 m^3/d and 0.020 m^3/d. The remaining 1% had a discharge of more than 0.020 m^3/d.

The infiltration rates for steady state conditions (0 to 0.09 m/d) were larger than the average infiltration rates for transient conditions (0 to 0.032 m/d). The water level of the Petit Buëch river and the related hydraulic heads had an effect on the infiltration rates and locations. Furthermore, the infiltration rates for transient conditions were achieved by modeling for 365 days and not for one day as for steady state conditions.

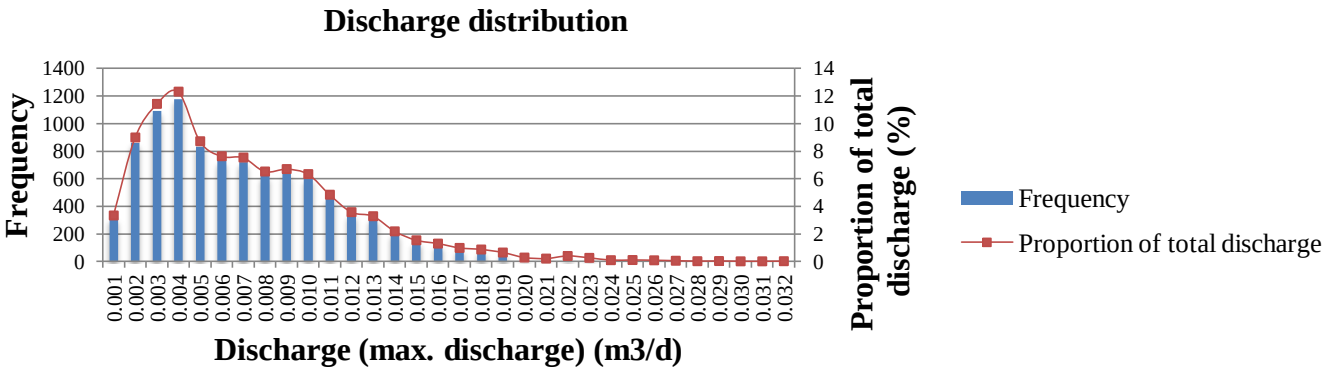

Figure 3.29: Histogram of the discharge distribution and graph of the proportion of total discharge for transient conditions.

The pattern of the average residence time distribution for transient modeling was less clear than for the average infiltration rates (figure 3.30). However, residence times of more than 200 days were mostly found at the north-east and south-west. Most short residence times of less than 200 days occurred at the west side of the point bar.

Particles which infiltrated with a small infiltration rate were trapped in the point bar and had a relatively long residence time. In addition, particles with large infiltration rates had a relatively short residence time. Due to the changing water level of the Petit Buëch river the particles in the point bar moved alternately from and to the river. Therefore, infiltrated particles did not travel large distances through the point bar but travelled for only a few meters before seepage into the river occurred. As a consequence, most subsurface water in the

point bar was not directly affected by river water. The transient part of this research only studied particles which were released from the main interface between the point bar and the Petit Buëch river (figure 3.30). If the side streams were also accounted there would also be infiltration from the side streams into the point bar. Water and solutes which infiltrated from side streams would also have had an effect on the subsurface water of the point bar.

For both steady state and transient conditions the longest residence times were found in the north-east. For steady state conditions those residence times were mainly between 600 days and 900 days while for transient conditions the average residence times ranged from 200 days to 1100 days. However for transient conditions the residence times (figure 3.30) were an average for the modeling period of one year.

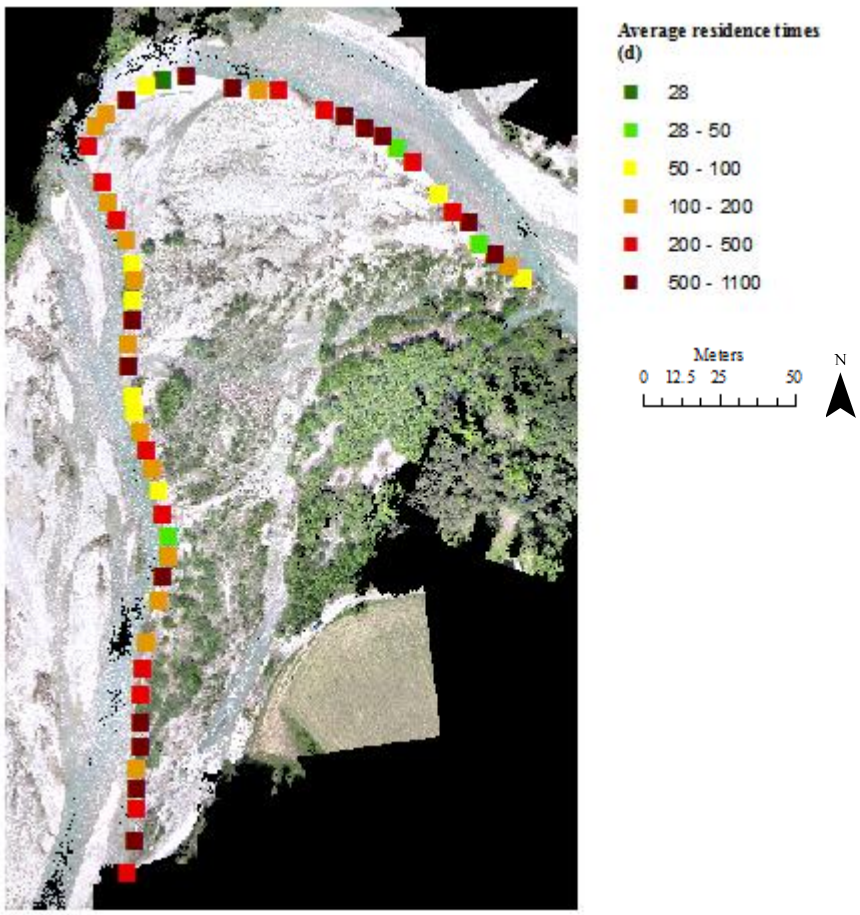

Figure 3.30: Map of the average residence time distribution for the study area. The given residence time for each cell is the average obtained for one modelled year.

The residence times ranged from 1 to 1079 days with about 50% of the total residence times between 1 and 100 days (figure 3.31). The frequency curve decreased from 100 to 150 days

and increased again to 350 days. After 350 days the frequency curve decreased again. Long residence times between 600 days and 850 days resulted in a frequency peak which contained approximately 10% of the total residence times.

Due to a restriction of Modflow the total modeling time was 1080 days. Therefore, when a particle reached a residence time beyond the modeling time, modeling stopped. For example: a particle released on day 1 was able to have a maximum residence time of 1080 - 1 = 1079 days. Likewise, a particle released on day 365 was able to have a maximum residence time of 1080 – 365 = 715 days. As a result, the residence time distribution could have had contained longer residence times. However, the number of particles which could have had a longer residence time would be less than 1% of the total residence times (figure 3.31).

The residence time distributions for steady state and transient conditions both had a frequency peak between 650 days and 850 days. Those long residence times occurred in the north-east were the infiltration rates were low.

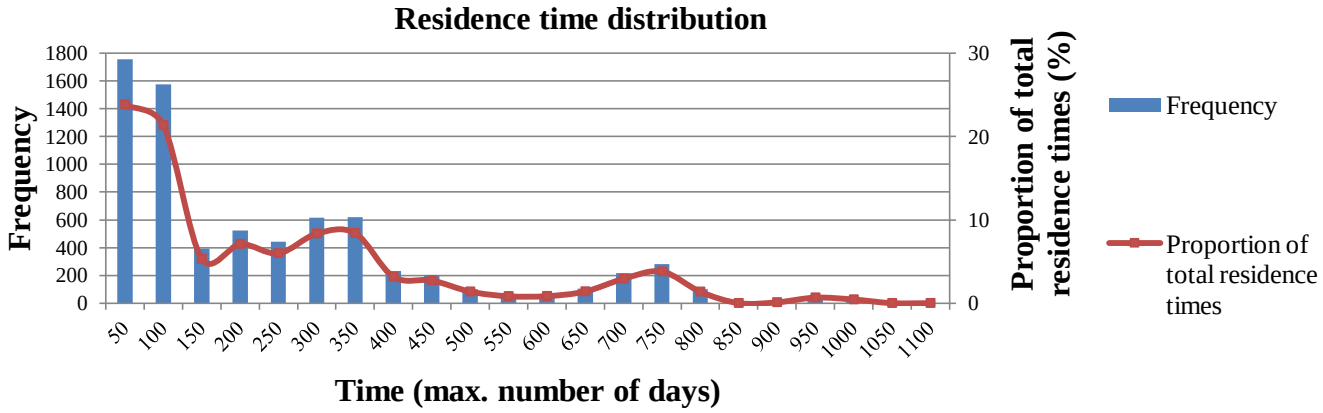

Figure 3.31: Frequency histogram of the residence time distribution and graph of the proportion of total residence times for transient conditions.

Figure 3.32 shows the hyporheic exchange rate versus the residence time for transient conditions. In general, a smaller hyporheic exchange rate resulted in a longer residence time. This relation between hyporheic exchange rates and residence times was:

$$Q_{HE} = -0.000003 * RT + 0.0081 \quad (15)$$

The coefficient of determination was 0.0266, which is very low. This can be explained by the large variation in hyporheic infiltration rates and their related residence times due to the

varying morphology throughout the study area and the varying water level. As could be seen from figures 3.28 and 3.30 the hyporheic exchange rate (infiltration in this case) was not clearly related to the residence time. A larger hyporheic exchange rate occurred at approximately 50, 300, and 700 days (figure 3.32).

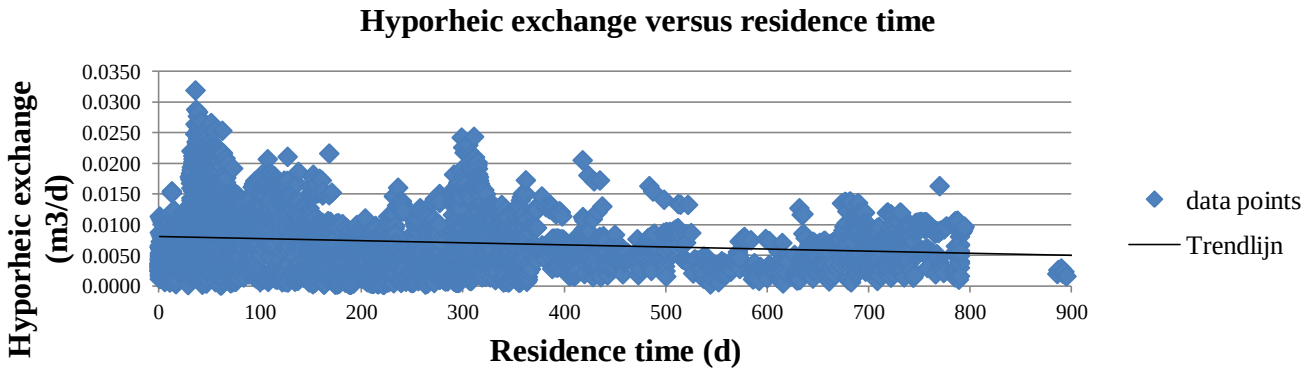

Figure 3.32: Graph of the hyporheic exchange rate plotted against residence time for transient conditions.

3.3 Hyporheic exchange and residence times

To determine whether there was a relation between the results of the uranine experiments, the residence time distribution for steady state modeling, and the residence time distribution for transient modeling, a conversion was done whereby the discharge fractions were determined. This fraction represents the quantity of surface water which is withdrawn from the river and is converted to subsurface flow.

The river discharge (Q_{river} ; m^3/d) for uranine experiment 1 was equal to 601840 m^3/d and for uranine experiment 2 equal to 409973 m^3/d (section 3.1.4). The discharge fractions for the uranine measurements were also determined by the measured concentration for a time step ($C_{\Delta t}$; g/m^3), the time step (Δt ; d), and the total mass (M; g):

$$\text{discharge fraction} = \frac{Q_{river} * C_{\Delta t} * \Delta t}{M} \quad (16)$$

To obtain the discharge fractions for the modeled residence time distributions, the hyporheic exchange rates were divided by the Petit Buëch river discharge. For steady state modeling, the river discharge during the first uranine experiment, which was used at this experiment, was performed closest to the modeled period.

The discharge fractions and residence times were plotted on a normal scale (figures 3.33, 3.34, and 3.35) in order to observe the relation between the uranine experiments and the modeled residence time distributions. Trendlines were drawn through the observation and modeled points whereby the relation between the discharge fractions and modeled residence times for steady state conditions was:

$$\frac{Q_{HE}}{Q_{river}} = 4.0 * 10^{-8} * RT^{-0.261} \quad (17)$$

And for transient conditions:

$$\frac{Q_{HE}}{Q_{river}} = -4.0 * 10^{-6} * RT + 0.0053 \quad (18)$$

The coefficients of determinations were 0.943 (uranine experiment 1), 0.995 (uranine experiment 2), 0.357 (steady state), and 0.050 (transient). The coefficients of determination for the uranine experiments were high, indicating little deviation from the mean. In contrast, the coefficient of determination for the modeled residence time distributions were much smaller due to much deviation from the mean.

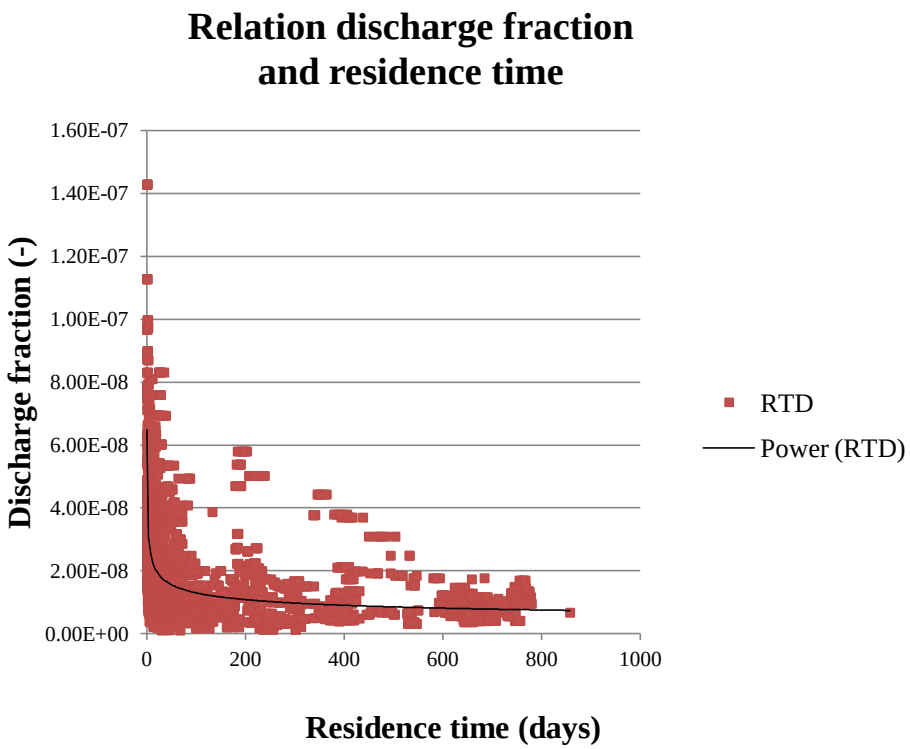

Figure 3.33: Graph of the relation between the discharge fraction and residence time obtained by steady state modeling.

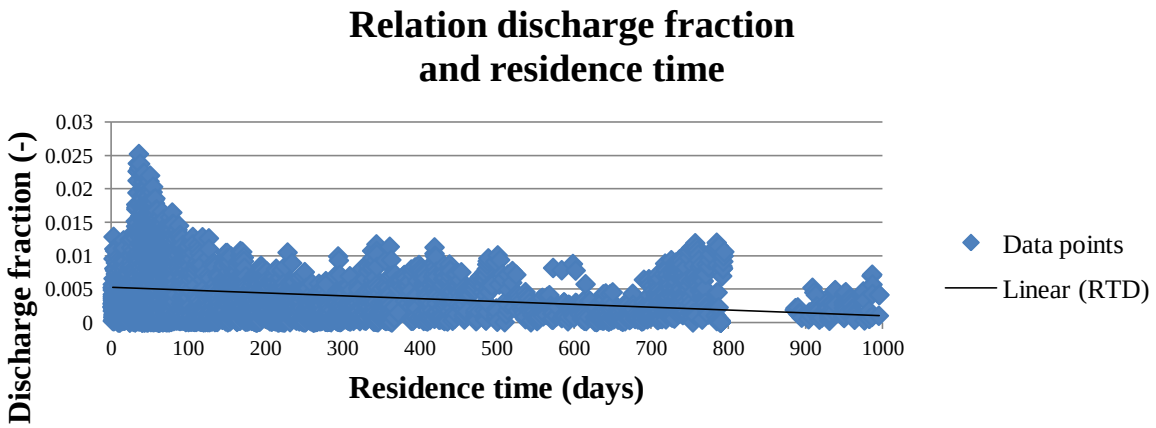

Figure 3.34: Graph of the relation between the discharge fraction and residence time obtained by transient modeling.

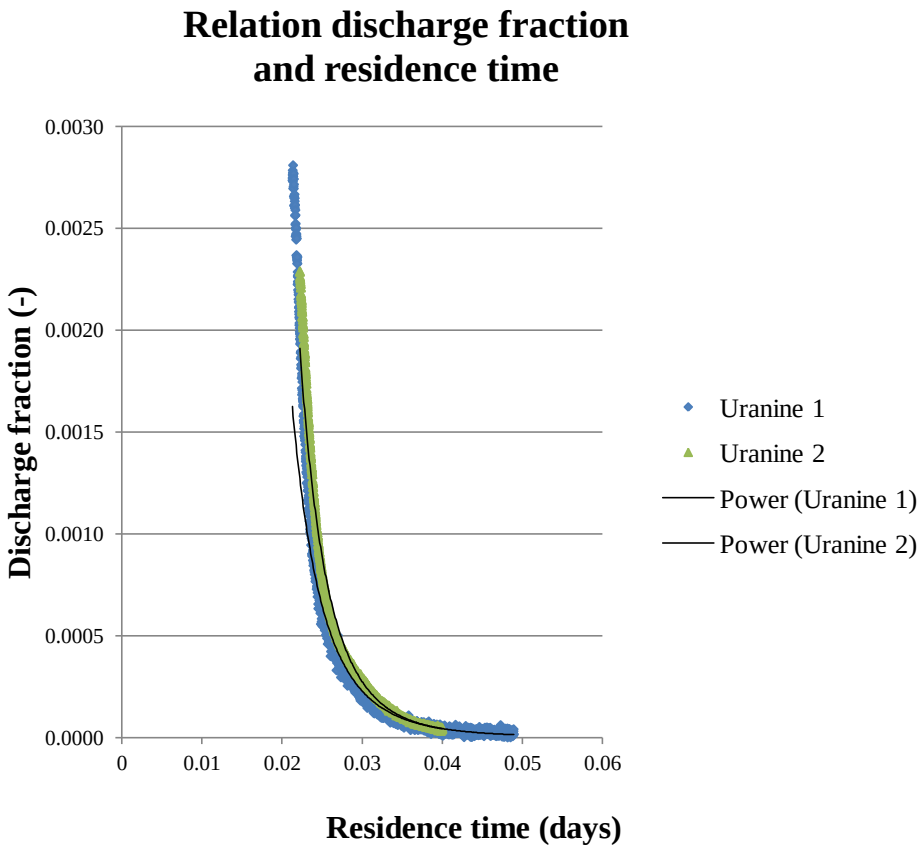

Figure 3.35: Graphs of the relation between the discharge fraction and residence time obtained by the uranine experiments.

For each day the discharge fractions were summed to determine the relation between the river discharge and river water infiltration in the point bar. The sum of the discharge fractions for steady state conditions was 0.0001. Therefore, 0.01% of the total river discharge infiltrated the hyporheic zone.

For transient conditions, the sum of the discharge fractions, during one year, ranged from zero to 0.59 (figure 3.36). Furthermore, the river discharge ranged from almost zero to 2826576 m^3/day. A small river discharge resulted in large sum discharge fractions (relatively much river water infiltration into the point bar). Likewise, a large river discharge resulted in a small proportion of infiltration into the hyporheic zone. A trendline was drawn through the data points of figure 3.36. The relation between river water infiltration and river discharge (Q_{river}) could be represented as:

$$\text{sum discharge fractions} = 4*10^{8} * Q_{river}^{-1.861} \quad (19)$$

The trendline of figure 3.36 had a coefficient of determination equal to 0.72. The deviations from the general trend are mainly caused by differences between the rising limb of the hydrograph (relatively much infiltration) and the falling limb of the hydrograph (relatively little infiltration).

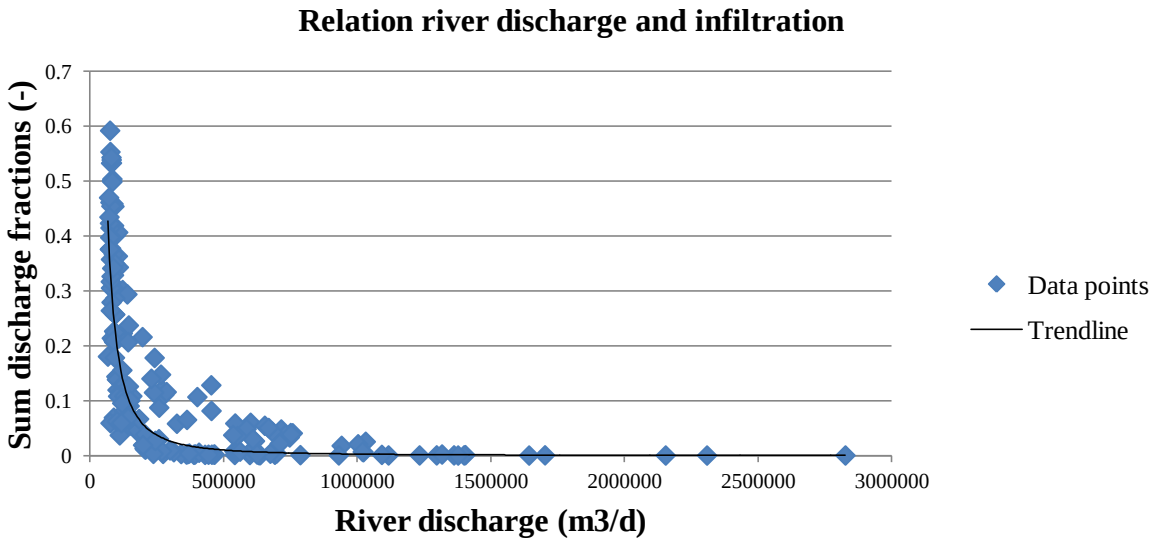

Figure 3.36: The relation between the proportion of river water infiltration and the river discharge for transient conditions.

Figure 3.37 shows the sum discharge fractions in relation to the modeled time. For example, the month April was dominated by a large river discharge whereby a small proportion of river water infiltrated the point bar. During June the river discharge was relatively small resulting in river water infiltration into the point bar ranging between 40% and 60%. At the start of the fieldwork period (end May) a high water level and large flow velocity was observed. Furthermore, during June the water level of the river and the hydraulic heads decreased. During this period a net outflow of hyporheic water occurred. The river discharge was large (figure 3.37) but the amount of infiltration was small. During large river discharges, river water and solutes had a large flow velocity (Hendriks, 2010) and the amount of infiltration was small. Furthermore, during small river discharges the flow velocity decreased whereby infiltration of solutes into the sediments of the point bar occurred.

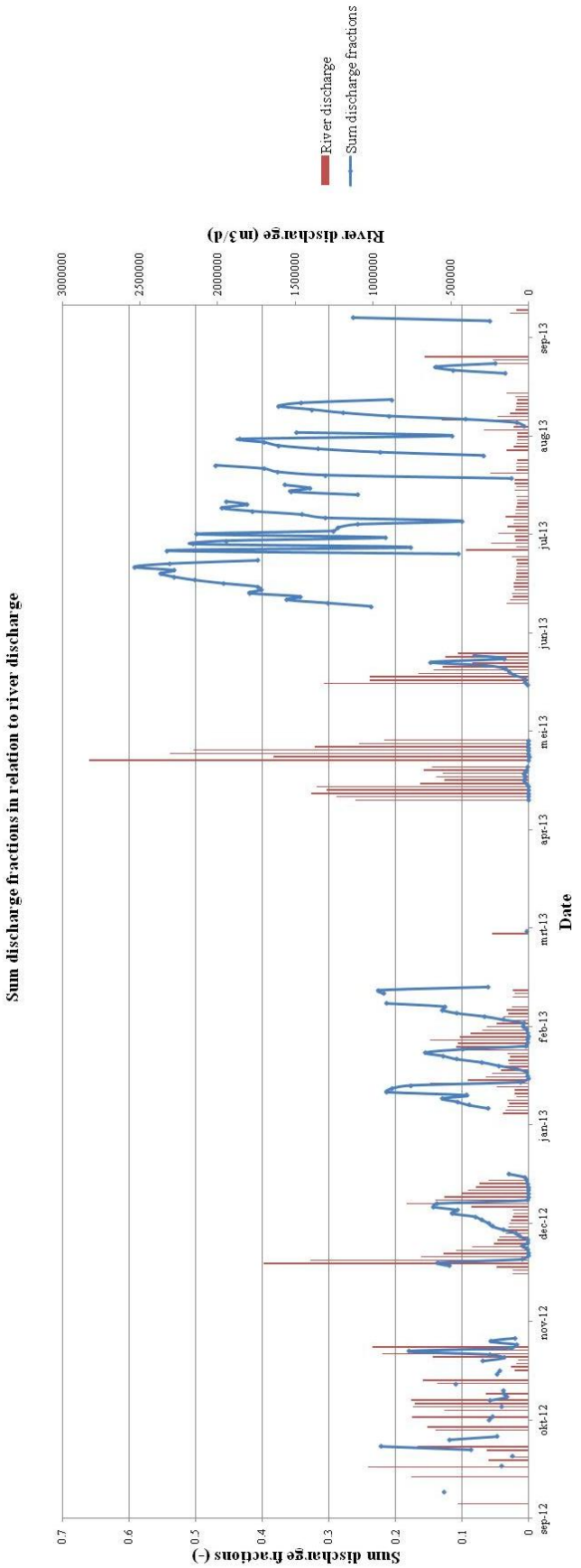

Figure 3.37: Infiltration proportions during one year. The amount of river discharge is also given.

The discharge fractions and residence times for transient conditions were plotted on a log-log scale in figure 3.38. To this figure the discharge fractions and residence times for steady state conditions, and the relation between the discharge fraction and residence time obtained by the uranine experiments were added.

The residence times obtained by the uranine experiments varied from 0.021 to 0.049 days and the discharge fractions varied from $4.6*10^{-5}$ to 0.0023, which was much less than the modeled residence times and discharge fractions. Furthermore, the trendline of the uranine log-log graphs shows a steeper slope than for the modeled residence time. The steeper slope of the uranine log-log graphs indicate that the ratio between residence time and infiltration quantity is smaller, indication that the infiltrated water had shorter residence times.

Both uranine graphs represent: 1) flow velocity differences in the river channel; 2) temporary storage in dead zones and side channels; 3) quick hyporheic exchange due to bed forms. The velocity differences occur between the centre and banks of the river channel and between the surface and bottom. The graphs of the modeled residence time distributions represent only the transport of water and particles through the hyporheic zone.

The residence times for steady state modeling varied from 5 hours to 857 days and for transient modeling from 1 day to 1079 days.. The discharge fractions of the steady state modeled residence times varied from $1.02*10^{-9}$ to $1.42*10^{-7}$, while the discharge fractions for transient modeling varied from 0 to 0.025. Both steady state and transient graphs represented the transport of water and solutes through the hyporheic zone of the point bar. The residence times of transient modeling were longer due to the travel paths taken by the infiltrated particles. With steady state modeling the particles travelled a long distance through the point bar before seepage occurred into the river. For transient modeling, infiltrated particles did not travel large distances through the point bar but travelled for only a few meters. This is due to the fluctuations in the river discharge, water levels and hydraulic heads during the year, which causes a more intense hyporheic exchange between river water and groundwater. There are days that as much as 59% of the river discharge infiltrates into the hyporheic zone, although the residence times of the infiltrated water is relatively short.

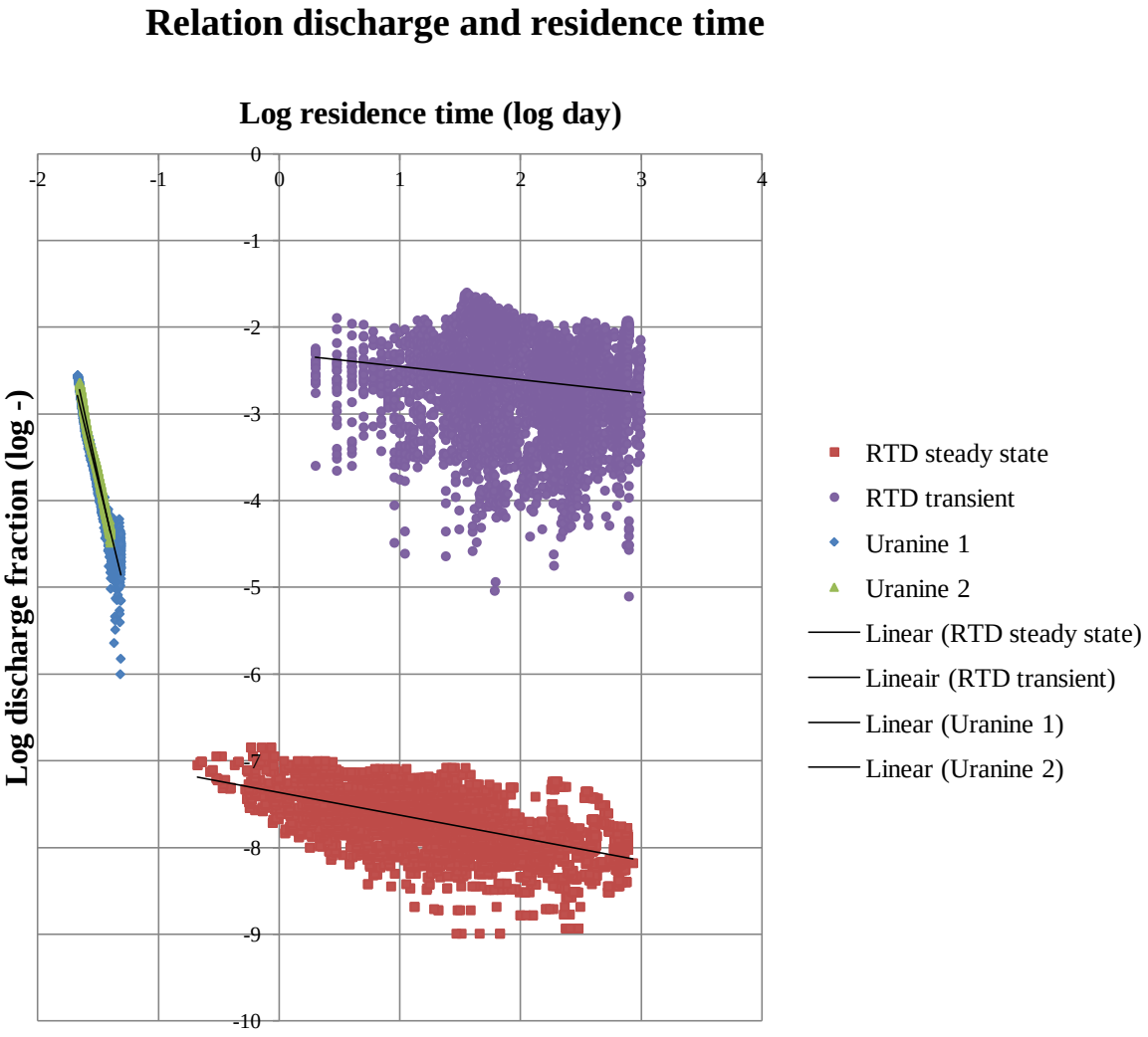

Figure 3.38: Graphs of the relation between the discharge fraction and residence time on a log-log scale.

Chapter 4 Conclusion

At the interface of surface water and subsurface water infiltration from or exfiltration into the Petit Buëch river occurred. Most infiltration occurred in the north-east of the point bar and those infiltrated particles had a relatively long residence time which could be more than 1000 days. Downwelling into the hyporheic zone occurred when the velocity of the hyporheic flow increased due to, for example, the increase in hydraulic conductivity or a high pressure zone. Upwelling occurred when the velocity of the subsurface flow reduced due to a reduction in hydraulic conductivity or when there was a low pressure zone. The model was calibrated for the hydraulic conductivity in order to agree with the measured hydraulic head data. The found hydraulic conductivity was equal to an average of 0.025 m/s. However, as a result of the inhomogeneity of the point bar, which consisted of a mixture of gravel and sand, locations more inland might have had a smaller hydraulic conductivity value.

Particles with a large hyporheic exchange rate had a short residence time whereas particles with a small hyporheic exchange rate had long residence times. With steady state modeling the particles travelled a long distance before seepage into the river occurred. With transient modeling the particles did not travel a long distance but remained in the vicinity of the surface and subsurface water boundary. The discharge and water level of the river fluctuated, resulting in a fluctuating hydraulic head distribution and a variable gradient. Due to the changing water level, during the period of 365 days, the flow direction of the subsurface water varied and the particles moved alternately from and to the river. Furthermore, the infiltration rates, and locations varied through time. As a consequence, most subsurface water in the point bar was not directly affected by river water. However, during high river discharge the point bar would be flooded and side channel would be created. If the side streams were also accounted with transient modeling there would have been infiltration from the side streams into the point bar.

During the conditions used for steady state modeling about 0.01% of the total river discharge infiltrated the hyporheic zone in the studied reach of the Petit Buëch river. For the transient modeling, there are moments that more than 50% of the total river discharge infiltrates into the hyporheic zone in the study area, although the residence times of the infiltrated water are generally much shorter. Nevertheless, this study shows that discharge variations during the year enhances hyporheic exchange and may considerable delay in chemical signals due to e.g. precipitation, industrial pollution, or agriculture releases.

References

Adams, E.E., Gelhar, L.W. (1991). Field study of dispersion in a heterogeneous aquifer: 2. Spatial moments analysis. Water resources research 48/12, p.3293-3307.

Beard, D.C., Weyl, P.K. (1973). Influence of texture on porosity and permeability of unconsolidated sand. AAPG Bulletin 57, p.349-369.

Boulton, A.J., Findlay, S., Marmonier, P., Stanley, E.H., Valett, H.M. (1998). The functional significance of the hyporheic zone in streams and rivers. Annual review of ecology and systematics 29, p.59-81.

Boulton, A.J. (2007). Hyporheic rehabilitation in rivers: restoring vertical connectivity. Freshwater Biology 52, p.632-650.

Brunke, M., Gonser, T. (1997). The ecological significance of exchange processes between rivers and ground-water. Freshwater biology 37, p.1–33.

Cardenas, M.B., Wilson, J.L., Zlotnik, V.A. (2004). Impact of heterogeneity, bed forms, and stream curvature on subchannel hyporheic exchange. Water resources research 40.

Cardenas, M.B. (2008). Surface water-groundwater interface geomorphology leads to scaling of residence times. Geophysical research letters 35.

Chiang, W.H., Kinzelbach, W. (1998). Processing Modflow. A Simulation system for modeling groundwater flow and pollution.

Debelmans, J. (1974). Géologie de la France. Paris, Masson et Cie, 540 pp.

Dieulin, A. (1980). Propagation de pollution dans un aquifer alluvial: L'effet de parcours, doctoral dissertation, Université Pierre et Marie Curie-Paris VI and L'Ecole Nationale Superieur des Mines de Paris, Fontainebleau, France.

Fitts, C.R. (2002). Groundwater science. Academic press, Amsterdam.

Freeze, R.A. and J.A. Cherry. (1979). Groundwater, Prentice Hall, Englewood Cliffs,N.J.

Fried, J.J., Ungemach, P. (1971). Determination in situ du coefficient de dispersion longitudinal d'un milieu poreux naturel. Academic. science 2/272, p.1327-1329.

Frings, R. M., Kleinhans, M.G., Vollmer, S. (2008). Discriminating between pore-filling load and bed-structure load: a new porosity-based method, exemplified for the river Rhine. Sedimentology 55, p.1571-1593.

Gaussen, H. (1970). Précipitations, temperatures et végétation des Alpes occidentales. Geobotanisches institut rübel Zürich 43, p.44-57.

Grimberg, T. (2013). Hyporheic Exchange in the Petit Buëch, Southern France.

Haggerty, R., Wondzell, S.M., Johnson, M.A. (2002). Power-law residence time distribution in the hyporheic zone of a 2nd-order mountain stream. Geophysical research letters 29/13.

Harbaugh, A.W. (1990). A program for calculation subregional water budgets using results from the U.S. Geological Survey's modular three-dimensional finite-difference ground-water flow model. U.S. geological survey. Open file report. 90-392, 27 pp.

Harvey, J.W., Bencala, K.E. (1993). The effect of streambed topography on surface-subsurface water exchange in mountain catchments. Water resources research 29/1.

Hendriks, M.R. (2010). Introduction to physical hydrology. Oxford university press, New York.

Konikow, L.F., Bredehoeft, J.D. (1974). Modeling flow and chemical quality changes in an irrigated stream-aquifer system. Water resources. Research, 10/3, p.546-562.

Larkin, R.G., Sharp, J.M. (1992). On the relationship between river-basin geomorphology, aquifer hydraulics, and ground-water flow direction in alluvial aquifers. Geological society of America bulletin 104/12, p.1608-1620.
Loke, M.H. (1999). Electrical imaging surveys for environmental and engineering studies: a practical guide to 2-D and 3-D surveys. User's Manual for Res2dinv.
Maloszewski, P., Zuber, A. (1982). Determining the turnover time of groundwater systems with the aid of environmental tracers. 1. Models and their applicability. Journal of Hydrology 57, p.207-231.
Marsily, de, G. (1986). Quantitative hydrogeology: groundwater hydrology for engineers. San Diego: Academic Press.
McDonald, M. G., and A. W. Harbaugh (1996). Programmer's documentation for MODFLOW-96, an update to the U.S. Geological Survey modular finite-difference ground-water flow model, U.S. Geological survey. Open file report, 96-486, 220 pp.
McGuire, K.J., McDonnell, J.J. (2006). A review and evaluation of catchment transit time modeling. Journal of Hydrology 330, p.543-563.
Meyzeng, C. (1984). Hautes-Alpes, Ubaye, Haut-Drac, Préalpes drômoises. Pays de transition enter Alpes du Nord et Alpes du Sud. 954 p. Editions OPHRYS Gap.
Morrice, J.A., Valett, H.M., Dahm, C.N., Campana, M.E. (1997). Alluvial characteristics, groundwater-surface water exchange and hydrologic retention in headwater streams. Hydrological Processes 11, p.253-267.
Packman, A. I., and K. E. Bencala (2000). Modeling surface-subsurface hydrological interactions, in streams and ground waters, edited by J. B. Jones and P. J. Mulholland, p. 45– 80, Academic press, San Diego California.
Pollock, D. W. (1994). User's guide for MODPATH/MODPATH-PLOT, version 3: A particle tracking post-processing package for MODFLOW, the U.S. Geological Survey finite-difference ground-water flow model, U.S. geological survey. Open file report, 94-464, 234 pp.
Salehin, M., Packman, A.I., Paradis, M. (2004). Hyporheic exchange with heterogeneous streambeds: Laboratory experiments and modeling. Water resources research 40.
Sandre (2011). Service d'administration nationale des données et référentiels sur l'eau. Fiche cours d'eau le Petit Buëch.
Sophocleous, M.A. (2002). Interactions between groundwater and surface water: the state of the science. Hydrogeology journal 10, p.52-67.
Telford, W.M., Geldart, L.P., Sheriff, R.E. (1990). Applied geophysics. Second edition. Cambridge university press, Cambridge.
Tonina, D. (2005). Interaction between river morphology and intra-gravel flow paths within the hyporheic zone. Unpublished Ph.D. dissertation, Boise, ID: University of Idaho.
Tonina, D., Buffington, J.M. (2009). Hyporheic exchange in mountain rivers I: Mechanics and environmental effects. Geography Compass 3/3 p.1063-1086.
U.S. Environmental protection agency. Environmental geophysics: electrical methods.
Wolock, D.M., Fan, J., Lawrence, G.B. (1997). Effects of basin size on low-flow stream chemistry and subsurface contact time in the Neversink river watershed, New York. Hydrological processes 11, p.1273-1286.
Wörman, A., Packman, A.I., Johansson, H., Jonsson, K. (2002). Effect of flow-induced

exchange in hyporheic zones on longitudinal transport of solutes in streams and rivers. Water resources research 38/1.

Appendix A.

Groundwater and surface water level data

Measurement point	Water level with respect to NAP (m) Date 3-jun	10-jun	12-jun	14-jun	16-jun	18-jun	19-jun	6-jun	Decrease
gw1	750.49	750.45	750.43	750.43	750.42	750.40	750.40	750.48	0.10
gw2	750.98	750.90	750.84	750.82	750.81	750.79	750.76	750.95	0.21
gw3	751.19	751.17	751.17	751.17	751.17	751.16	751.16	751.18	0.04
gw4	751.50	751.48	751.47	751.45	751.46	751.47	751.46	751.49	0.04
gw5	751.75	751.73	751.71	751.73	751.72	751.71	751.71	751.74	0.04
gw7	750.30	750.26	750.22	750.21	750.18	750.19	750.17	750.29	0.13
gw8	750.41	750.38	750.36	750.36	750.35	750.34	750.32	750.40	0.09
gw10	751.86	751.81	751.78	751.78	751.77	751.76	751.75	751.83	0.11
gw11	751.95	751.90	751.88	751.86	751.86	751.86	751.85	751.92	0.10
gw12	752.28	752.25	752.23	752.23	752.22	752.21	752.21	752.25	0.07
gw13	752.31	752.27	752.25	752.24	752.24	752.23	752.22	752.30	0.10
gw14	752.41	752.35	752.34	752.32	752.32	752.32	752.29	752.38	0.12
gw15	752.71	752.66	752.64	752.63	752.62	752.61	752.61	752.67	0.10
gw16	752.52	752.47	752.45	752.44	752.43	752.42	752.40	752.50	0.12
gw17	752.59	752.53	752.51	752.50	752.49	752.48	752.46	752.57	0.13
gw18	752.64	752.58	752.55	752.54	752.53	752.52	752.51	752.62	0.13
gw19	750.99	750.96	750.93	750.93	750.92	750.91	750.90	750.97	0.08
gw20	750.89	750.85	750.83	750.82	750.82	750.81	750.79	750.88	0.10
gw21	750.72	750.65	750.62	750.59	750.59	750.57	750.55	750.69	0.17
sw1	-	749.33	749.31	749.30	749.28	749.27	749.26	749.36	0.07
sw2	-	750.91	750.89	750.88	750.87	750.82	750.84	750.95	0.06
sw3	-	755.15	755.15	755.15	755.12	755.12	755.10	755.19	0.06

Two different lengths of monitoring wells were used: 155 or 197 cm. They had an inner diameter of 3.6 cm and an outer diameter of 4.6 cm. The holes for the inlet of water were situated between 13 and 29.5 cm from the bottom of the monitoring well.

Appendix B.

Salt tracer experiment breakthrough curves

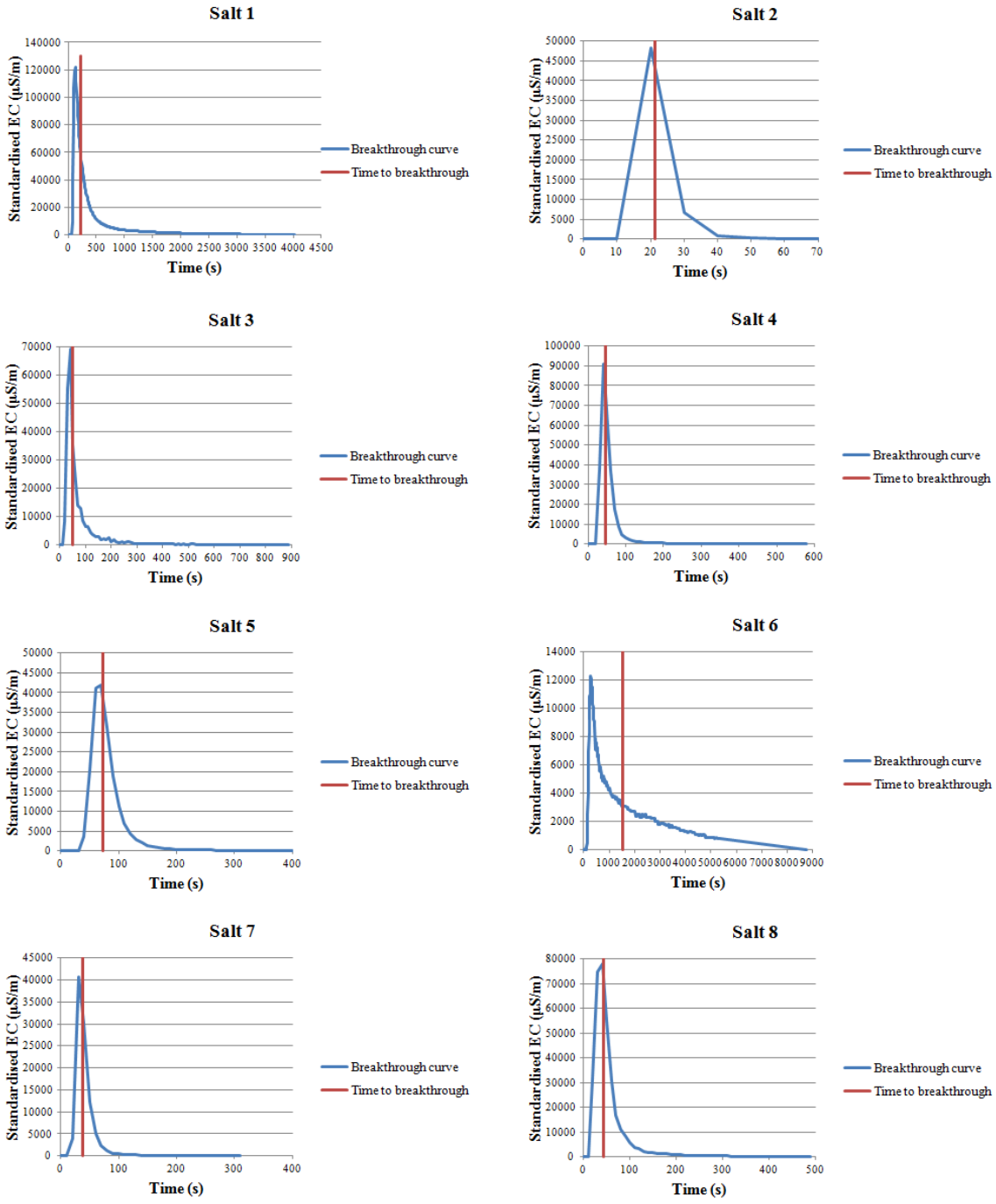

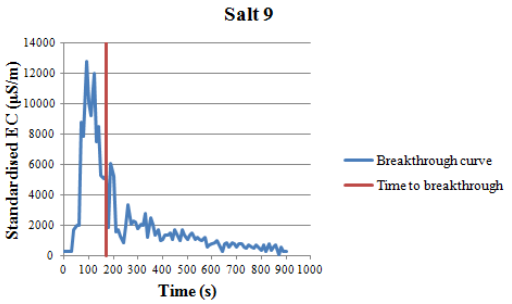
Salt 9
Standardised EC (µS/m)
Time (s)
Breakthrough curve
Time to breakthrough

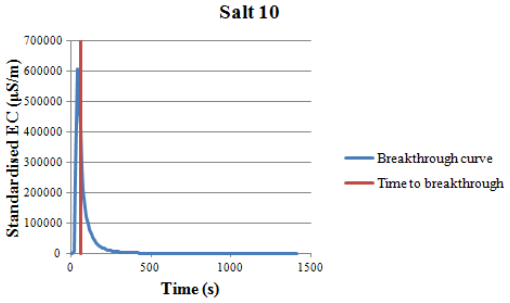
Salt 10
Standardised EC (µS/m)
Time (s)
Breakthrough curve
Time to breakthrough

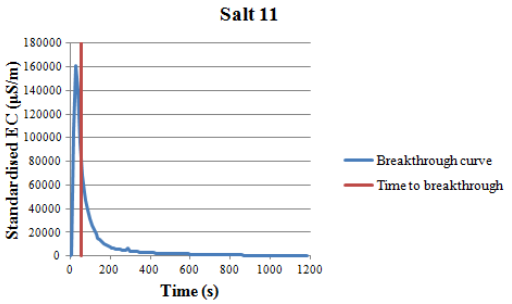
Salt 11
Standardised EC (µS/m)
Time (s)
Breakthrough curve
Time to breakthrough

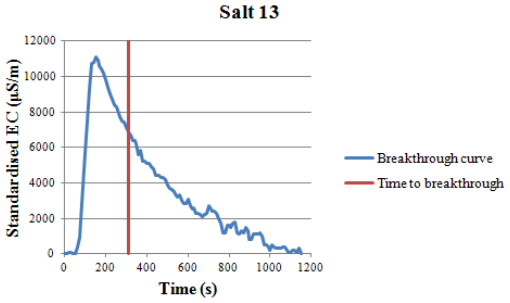
Salt 13
Standardised EC (µS/m)
Time (s)
Breakthrough curve
Time to breakthrough

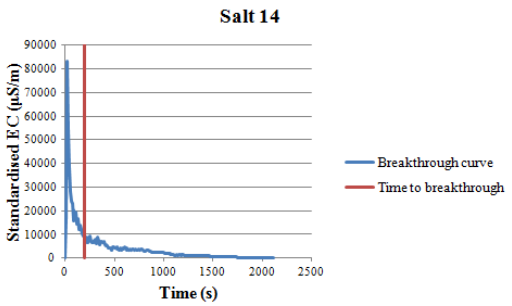
Salt 14
Standardised EC (µS/m)
Time (s)
Breakthrough curve
Time to breakthrough

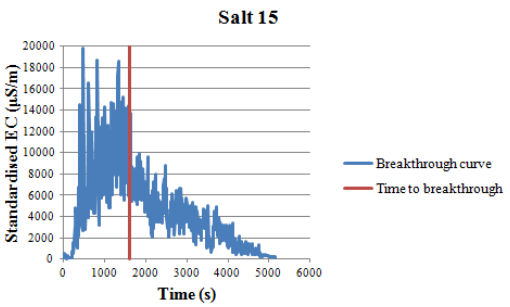
Salt 15
Standardised EC (µS/m)
Time (s)
Breakthrough curve
Time to breakthrough

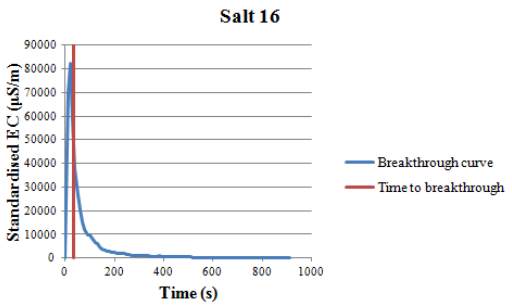
Salt 16
Standardised EC (µS/m)
Time (s)
Breakthrough curve
Time to breakthrough

Appendix C.
Flow velocity

The flow velocity curve for La Roche des Arnauds during the fieldwork period. From: Hydromet Group, OTT netView (www.ott.com)

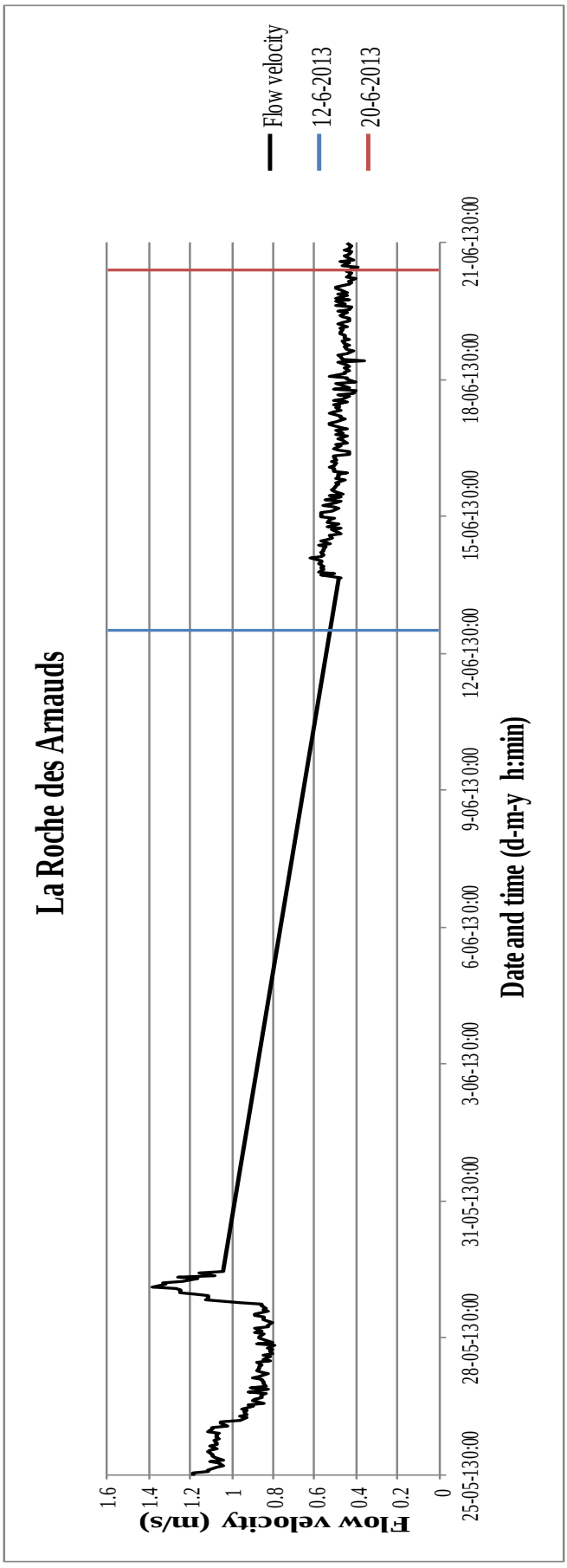

Appendix D.

Apparent resistivity

Apparent resistivity measurement 1			
s (m)	V (mV)	Ω (Ω)	pa (Ωm)
3.00	35.30	2.3600	64.87
3.50	34.00	1.7270	65.11
4.00	33.40	1.3060	64.62
4.50	32.50	1.0130	63.65
5.00	32.10	0.7900	61.43
5.50	31.80	0.6480	61.07
6.00	31.50	0.5160	57.95
6.50	31.50	0.4340	57.26
7.00	31.40	0.3630	55.59
7.50	31.10	0.3000	52.78
8.00	31.10	0.2400	48.07
8.50	30.90	0.2080	47.05
9.00	30.30	0.1830	46.42
9.50	30.40	0.1600	45.24
10.00	29.70	0.1370	42.93
11.00	35.90	0.1020	38.69
12.00	36.30	0.0790	35.68
13.00	35.70	0.0593	31.44
14.00	35.50	0.0460	28.29
15.00	36.00	0.0408	28.81
16.00	36.00	0.0289	23.22
17.00	36.70	0.0222	20.14
18.00	35.00	0.0179	18.21

Apparent resistivity measurement 2			
s (m)	V (mV)	Ω (Ω)	pa (Ωm)
3.00	22.60	2.8200	77.52
3.50	31.00	2.0100	75.78
4.00	25.10	1.5350	75.95
4.50	24.50	1.1980	75.27
5.00	25.80	0.9360	72.78
5.50	24.70	0.7330	69.08
6.00	26.20	0.5920	66.49
6.50	24.70	0.4700	62.02
7.00	24.80	0.3850	58.96
7.50	24.20	0.3200	56.30
8.00	23.90	0.2640	52.87
8.50	21.30	0.2220	50.22
9.00	22.70	0.1890	47.95
9.50	20.70	0.1580	44.67
10.00	22.90	0.1410	44.19

Appendix E.

dGPS measurement points

Locations of dGPS measurement points along water edges, surface water level measurement points, and groundwater level measurement points. These measurements points resulted in a interpolated hydraulic head distribution, which was used as initial condition for the steady state groundwater model.